

Technical Report sent
to Walter Acree in
April 1993.

1N-71
020107

NAG 2-1095

Signal Analysis of Helicopter Blade-Vortex-Interaction Acoustic Noise Data

James C. Rogers
Renshou Dai¹

March 20, 1998

JAN 02 1999
CASI

¹Electrical Engineering Department, Michigan Technological University

Abstract

Blade-Vortex-Interaction (BVI) produces annoying high-intensity impulsive noise. NASA-Ames collected several sets of BVI noise data during in-flight and wind tunnel tests. The goal of this work is to extract the essential features of the BVI signals from the in-flight data and examine the feasibility of extracting those features from BVI noise recorded inside a large wind tunnel.

BVI noise generating mechanisms and BVI radiation patterns are considered and a simple mathematical-physical model is presented. It allows the construction of simple synthetic BVI events that are comparable to free flight data. The boundary effects of the wind tunnel floor and ceiling are identified and more complex synthetic BVI events are constructed to account for features observed in the wind tunnel data. It is demonstrated that improved recording of BVI events can be attained by changing the geometry of the rotor hub, floor, ceiling and microphone.

The Euclidean distance measure is used to align BVI events from each blade and improved BVI signals are obtained by time-domain averaging the aligned data. The differences between BVI events for individual blades are then apparent. Removal of wind tunnel background noise by optimal Wiener-filtering is shown to be effective provided representative noise-only data have been recorded. Elimination of wind tunnel reflections by cepstral and optimal filtering deconvolution is examined. It is seen that the cepstral method is not applicable but that a pragmatic optimal filtering approach gives encouraging results.

Recommendations for further work include: altering measurement geometry, real-time data observation and evaluation, examining reflection signals (particularly those from the ceiling) and performing further analysis of expected BVI signals for flight conditions of interest so that microphone placement can be optimized for each condition.

Contents

1	Introduction	3
2	Analysis of BVI Noise Generating Mechanism	5
2.1	Introduction	5
2.2	Determine the BVI noise source locations	6
2.3	Computation of BVI Source Locations	8
2.4	BVI Noise Radiation Direction	12
2.4.1	Lateral directivity BVI noise	12
2.4.2	Longitudinal direction of BVI noise	12
2.4.3	Microphone location for maximum BVI	13
2.5	BVI waveform features	14
2.6	Synthetic BVI events	15
2.7	Comparison of synthetic and real BVI events	18
2.8	Effect of changing wind tunnel measurement geometry	19
3	BVI Feature Extraction by Time-domain Averaging	22
3.1	Introduction	22
3.2	Data alignment for the in-flight test results	22
3.2.1	Preliminary visual examination of the data	22
3.2.2	Data alignment algorithm	24
3.2.3	Processed results for flight condition A: No. 203	27
3.2.4	Processed results for flight condition B: No. 307	29
3.2.5	Processed results for flight condition C: No. 315	30
3.2.6	Comparison of the averaged BVI waveforms from different blades and at different flight conditions	32
3.3	Data alignment for the wind tunnel test data	33
3.3.1	Preliminary visual examination of the data	33
3.3.2	Processed results for flight condition A: No. 39.24	34
3.3.3	Processed results for flight condition B: No. 48.19	35
3.3.4	Processed results for flight condition C: No. 48.18	36
3.3.5	Comparison of the averaged BVI waveforms from different blades and at different wind tunnel flight conditions	38
3.4	Comparison of the in-flight test data with the wind tunnel test data case by case	39

4	Further Processing and Analysis of the Wind Tunnel Test Data	44
4.1	Remove the wind tunnel background noise by optimal filtering	44
4.1.1	Design the noise-cancelling optimal filter	45
4.1.2	Filtered result for test condition A:39_24	46
4.1.3	Filtered result for test condition B:48_19	48
4.1.4	Power spectra of $x(n)$ and $w(n)$ and their relation to the optimal filter performance	49
4.2	Remove wind tunnel echos by deconvolution	53
4.2.1	Echo removal by cepstral deconvolution	55
4.2.2	Deconvolving wind tunnel data with an optimal linear filter	58
5	Conclusions and Suggestions for Further Work	65
5.1	Conclusions	65
5.2	Suggestions for Further Work	67

Chapter 1

Introduction

This research is carried out for and funded by NASA-Ames Research Center. The task is to analyze and process the six sets of helicopter blade-vortex-interaction (BVI) noise data provided by NASA-Ames. Half of the data sets are from in-flight tests and another half are from wind tunnel tests. The ultimate goal is to determine the feasibility of using the large 80x120 feet wind tunnel of NASA-Ames as an effective way to study the helicopter BVI signal.

Blade-vortex-interaction (BVI) is not just a problem of helicopters, it is a problem inherent in all rotor propulsion systems. When the rotor blade sweeps through the air (or water), the air at the front edge of the blade is split into two portions, one going up and over the blade and one going under the blade. At the blade's trailing edge the two rejoin and vortices are generated. Blade-vortex-interaction (BVI) occurs if another blade cuts through the vortex generated by the preceding blade. This BVI encounter produces high-intensity impulsive noise. When a helicopter is in forward descending flight, the following blades will break up the vortices generated by preceding blades, thus creating very strong BVI noise.

There are many reasons to study BVI and BVI acoustic noise. In the case of helicopters BVI encounters affect the blade lift, therefore affecting the stability and operation of the helicopter. Studying BVI noise can aid rotor and blade design and hence improve helicopter performance. Another reason is the physiological effect of the noise. BVI noise can be the strongest and most annoying portion of helicopter acoustic spectra so studying and consequently reducing the noise can make helicopter applications less intrusive.

The first step in studying BVI noise is of course to find proper ways to measure it. The easiest way appears to be using a helicopter scale model and testing it inside a wind tunnel. This was done from the 1960's to the 1980's, until the scalability of the BVI noise was questioned. It's easy to scale the geometric size of the helicopter but it's difficult to scale the flight conditions in order to obtain the same BVI signature. Now it's been accepted that the BVI noise is not scalable.

Another way of measuring BVI noise is an in-flight test such as that by NASA-Ames where a small quiet YO-3A airplane flies at a selected speed in front of the helicopter in a forward down and right position. Microphones are located on the tail and wing tips of the airplane. The helicopter pilot attempts to maintain a fixed separation distance and angular relation between the aircraft while acoustic data are acquired. The practical problems with this method are that it is very difficult to maintain constant aircraft and rotor speeds while

keeping the physical relationship fixed. The data acquired during in-flight tests usually contain significant random variations from one rotor revolution to another. Another problem is the high cost of the method.

The large wind tunnel at NASA-Ames, with a cross-section of 80x120 feet, offers the opportunity to do controlled BVI measurements using an unscaled rotor blade. Reflections and the background noise caused by the large fans that are used in the tunnel provide the most significant differences between in-flight and tunnel BVI data. The main task of this research is to identify and remove wind tunnel effects on BVI signals and thereby improve the feasibility of measuring BVI noise inside the wind tunnel.

In the next chapter (Chapter 2), we first analyze the noise generating mechanisms of the BVI signal. A simple mathematical-physical model is presented for characterizing and simulating the BVI impulsive noise generated by a four-bladed helicopter rotor. The model is used to determine the spatial locations where one blade will likely interact with the rotor tip vortices shed downward by preceding blades. These are the BVI noise source locations. Dependence of the source locations on some of the flight conditions is examined and the impulsive nature of the BVI noise is analyzed. Synthetic BVI events are generated and compared with the BVI acoustic data measured in the wind tunnel to gain further understanding of the boundary effects of the wind tunnel test environment. It is shown that changing the measurement geometry from that used for the data analyzed offers promise of more complete removal of wind tunnel reflections.

In Chapter 3, we use the time-domain averaging method to extract the essential BVI signal features (waveforms) from the measured data of many revolutions. The most critical issue of averaging is proper data alignment. This issue is solved by using the minimum distance algorithm to correctly align the BVI events from different revolutions. After obtaining the averaged BVI data sequence, comparisons are made to examine the variations of BVI events due to individual blades. Also, the variations of BVI events under different test conditions and the similarities and differences between the in-flight test results and the wind tunnel test results under similar flight conditions are considered.

In Chapter 4, we focus on the processing and analysis of the wind tunnel data. An optimal linear filter is designed to remove the wind tunnel background noise from the measured BVI data. The performance of this optimal filter is found to depend on the validity of the assumption that the ideal BVI signal is uncorrelated with the background noise. Filter performance is also seen to depend on the quality of the background noise measurement. After removing background noise, two ways of removing wind tunnel reflections are discussed. The first is by cepstral deconvolution, which is elegant but because of standard assumptions it lacks the ability to handle the real BVI data sequence. The second is an optimal linear deconvolution filter, which is more pragmatic and stable although less elegant. The deconvolved data sequence contains a minimal amount of echos, and is comparable with the in-flight test results, thus demonstrating the feasibility of using the wind tunnel as a way to measure the BVI signal from an unscaled model.

Chapter 5 presents conclusions and recommendations for future work.

Chapter 2

Analysis of BVI Noise Generating Mechanism

2.1 Introduction

The main task of this research is to process and analyze the measured helicopter BVI noise data. However, better data-processing algorithms are often dependent on understanding the details of the physical mechanisms that generated the data. Therefore in this chapter we first analyze the BVI signal generating mechanism. Also, understanding the physical mechanisms aids estimating the BVI source locations and the noise radiation patterns.

Previous research efforts on BVI have been remarkable although real progress comes slowly. Owing to the complex nature of BVI phenomenon. Naturally, it's been many researcher's dream to build a mathematical model that can simulate (or even predict) the interactions of a blade with a vortex and the generation of acoustic fields induced by the interaction. Relatively speaking, the research on the fluid mechanics aspect of BVI is quite successful [1], but the research on understanding the acoustic fields generated by BVI has had rather limited success. In this regard, *Lyrantzis and Xue* [2] compared a nonlinear aerodynamic code (VTRAN2) with *Kirchhoff's* method. But their report lacks a comparison with real measurement data. *Gallman* made a parametric computational study of isolated blade-vortex interaction noise [3]. *Schmitz and Yu* presented a rather comprehensive review on helicopter rotor impulsive noise [4]. Their paper covers both high-speed impulsive noise and BVI noise. Also comparison was made between a scaled model and a full-sized model. But their analysis is limited to a two blade rotor system.

In this chapter, we present a simple mathematical-physical model for characterizing and simulating the BVI impulsive noise generated by a four-bladed helicopter rotor. The model is based on simple geometric relations. Much of the aerodynamic and fluid mechanics details are ignored as these details are beyond the scope of this work. In the following sections, we first present a model for determining the spatial locations where one blade will likely interact with the vortex shed downward by preceding blades. Intuitively, these interaction locations are also the BVI noise source locations. It is shown that the simple model produces a sequence of blade-vortex interaction events having timing suitable for constructing reasonable synthetic BVI waveforms. The dependence of the BVI noise source locations on the flight conditions

is then illustrated. After this, an examination of the impulsive BVI waveform features is presented and the radiation directivity is considered. The analysis is extended to the space both below and above the rotor plane in order to fully account for the wind tunnel reflections from the floor and ceiling.

Following the above, an individual wavelet is postulated which, when convolved with the blade tip-vortex interaction events developed from the geometric model, produces a synthetic BVI waveform which compares favorably with a free flight waveform. Finally, ray tracing is applied to the known wind tunnel geometry to identify the relative timing of significant multi-path events and this timing is used with the synthetic BVI waveform to produce a multi-component synthetic waveform. This synthetic waveform, which demonstrates the principal features of the measured BVI events in the wind tunnel, is used as a basis for suggesting alternative experiment geometries which would minimize contamination of the desired direct path BVI event by wind tunnel reflections.

2.2 Determine the BVI noise source locations

It's been well accepted that the BVI noise source locations are simply the spatial 'points' where one or several blades interact with the vortex shed downward by preceding blades [4]. Locating these points is crucial for understanding the acoustic radiation pattern of the BVI noise. The fact that BVI noise is composed of discrete sharp impulses suggests that the blades interact with the vortices only at certain discrete locations, although the vortices are generated continuously. In the following, we present an analytical model to compute these interaction locations. The model is based on simple geometric relations.

Related previous work are those of *Spletstoeser* [6] and *Marcolini* [7] *et al.* They presented numerous experimental measurements of the BVI encounter locations. *Schmitz* [4] mentioned the similarities between the rigid and free wake models for predicting the interaction locations. The model presented here is essentially the rigid wake model, where the vortex is assumed to be 'rigid' and the destruction and recombination process of the vortex are ignored [1].

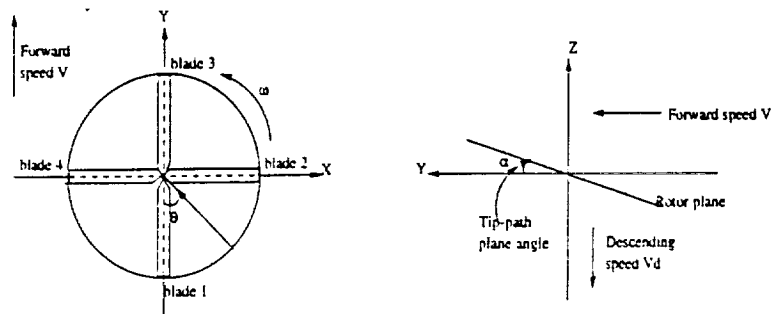


Figure 2.1: Coordinate system of the model. Left: Plan view of the rotor plane.
Right: Side view of the rotor plane.

Figure 2.1 shows the coordinate system used to describe the spatial locations of the blades. The left part of Figure 2.1 is the plan view of the rotor plane, whereas the right

part of Figure 2.1 is the side view of the rotor plane. The Figure shows the time instant $t = 0$ when the center of the rotor plane is coincident with the center of the coordinates. As time goes on, the rotor moves forward (along the Y-axis) with speed V (ground speed) and downward with speed V_d (descent rate). The blades are numbered as in Figure 2.1 for the instant $t = 0$. At any other instant $t = t_n$, the rotor tip location of blade n ($n = 1, 2, 3, 4$) is described by the following equations:

$$\begin{aligned}x_n &= R \sin(\omega t_n + (n - 1) \frac{\pi}{2}) \\y_n &= V t_n - R \cos(\omega t_n + (n - 1) \frac{\pi}{2}) \cos(\alpha - \gamma) \\z_n &= -V_d t_n - R \cos(\omega t_n + (n - 1) \frac{\pi}{2}) \sin(\alpha - \gamma)\end{aligned}\tag{2.1}$$

where R is the blade length (radius of the rotor plane), ω is the angular velocity of the rotor and α is the tip-path-plane angle (the angle between the rotor plane and the stream-wise coordinate, y). The angle is positive when the rotor plane is tilted rearward). If the helicopter is descending at glide path angle, γ , Figure 2.1 is modified to include this feature and the angle between the rotor tip plane and horizontal xy plane becomes $\alpha - \gamma$. For example, if the glide path angle is 5 degrees and the rotor tip path plane angle is 6 degrees the rotor tip path plane is inclined rearward and displays a 1 degree rearward tilt with respect to the horizontal plane. The descending flight configurations, which are known to generate strong BVI events, are of particular interest in the data examined in this report. Consequently, the difference, $\alpha - \gamma$, is usually only a few degrees for these cases.

In most cases, the vortices are generated below the blades. It is therefore fair to assume that the trajectories of the vortices are the trajectories of the blade tips but displaced downward by a certain distance z_d . This displacement depends on the advance ratio and the tip-path-plane angle. For example, the location of the vortex generated by blade m at time instant $t = t_m$ is:

$$\begin{aligned}x'_m &= R \sin(\omega t_m + (m - 1) \frac{\pi}{2}) \\y'_m &= V t_m - R \cos(\omega t_m + (m - 1) \frac{\pi}{2}) \cos(\alpha - \gamma) \\z'_m &= -V_d t_m - R \cos(\omega t_m + (m - 1) \frac{\pi}{2}) \sin(\alpha - \gamma) - z_d\end{aligned}\tag{2.2}$$

Now the task is to find when (or equivalently, where) blade n encounters the vortex generated by blade m . To accomplish this task, we make use of the closest distance between the rotor tip trajectory of blade n and the trajectory of the vortex generated by blade m :

$$d(t_n) = \min_{t_m} [\sqrt{(x_n - x'_m)^2 + (y_n - y'_m)^2 + (z_n - z'_m)^2}]\tag{2.3}$$

Notice that the closest distance is only a function of t_n (not a function of t_m) since the vortex is presumed to lie in space awaiting interaction with a blade at time t_n . Of course the rotor structure (two blades, four blades etc.), the velocities, V , V_d and the rotational speed, ω ,

are factors accounting for the difference in time between when the vortex was generated and when it is struck by a blade tip. Note that this model does not include the fact that BVI events have been shown to be located not at the rotor tip but at radial distances on the order of 0.6 to 0.8 R from the rotor hub [6]. (However, even with this simplification, it is seen that the model produces relative timing between sequential blade-tip-vortex interactions that are adequate for constructing a complete BVI event from the sequential events) The task of locating the possible blade-tip-vortex encounter time (or spatial point) is then equivalent to finding a specific value of t_n so that $d(t_n)$ is minimal. Practically, only the azimuth angle (θ) of blade n when it encounters the vortex of blade m needs to be known. The relation between θ and t_n is:

$$\theta = \omega t_n + (n - 1) \frac{\pi}{2} \quad (2.4)$$

The BVI source location in terms of azimuth angle is then expressed by:

$$\theta_s = \underset{\theta(t_n)}{\operatorname{argmin}} d(t_n) \quad (2.5)$$

2.3 Computation of BVI Source Locations

In this section, some computation results are presented for the BVI source locations using the aforementioned equations. For the ease of comparison, the flight parameters are chosen from those given by *Yamauchi* [5]. More specifically, the parameters of flight 203 are chosen, in which the true speed is $V = 65.8 \text{ knots}$, the descending rate is $V_d = 748 \text{ ft/min}$, the blade length is $R = 22 \text{ ft}$, the advance ratio is $\mu = 0.164$, the tip-path-plane angle is $\alpha = 6.3 \text{ deg}$, the glide path angle is $\gamma = 6.5 \text{ deg}$, and the vertical displacement of the vortex center from the vortex-generating rotor tip is $z_d = 20 \text{ cm}$ [1]. For simplicity but with no loss of generality blade 1 is tracked. Intuitively, blade 1 will encounter the vortices shed downward by the other three blades (blade 2, 3 and 4). This intuition turns out to be true. Figure 2.2 shows how the rotor tip trajectory of one blade (blade 1 in Figure 2.1) sweeps close to the vortex generated the adjacent leading blade (blade 2 in Figure 2.1). The figure clearly shows two possible encounter locations between the tip of blade 1 and the vortex from blade 2. To better visualize the BVI locations, we plot in Figure 2.3 the distance $d(t_n)$ against the azimuth angle θ in polar form for the three combinations of blade 1 with blade 2, 3 and 4. The BVI source locations (in terms of θ) correspond to the angles where the curve is closest to the center (the notches where $d(t_n)$ is minimal). As is obvious in Figure 2.3, for any pair of blades, one BVI source location is in the advancing side ($90 > \theta_1 > 0$) and another BVI source location is in the retreating side ($360 > \theta_2 > 270$).

Experimental observations reveal that the BVI source locations strongly depend on the tip-path-plane angle, α , and the advance ratio μ . [8] To verify this, we computed the BVI source locations for various tip-path-plane angles and various advance ratios using the model discussed here. The results are shown in Figure 2.4. Since only the BVI noise in the forward direction is of interest, only the advancing side BVI locations are shown in Figure 2.4.

As is clear in the Figure, the interaction azimuth angles move somewhat closer to the 90 degree location as the tip-path-plane angle increases, but they move farther away from the

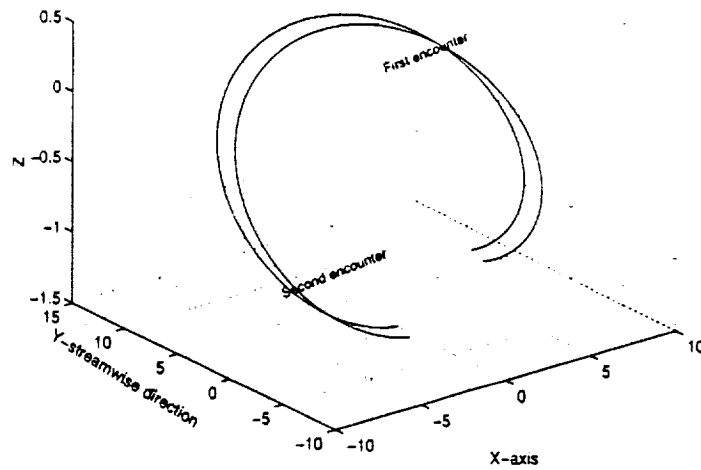


Figure 2.2: Trajectories of the vortex of blade 2 and the tip of blade 1. The figure shows two likely locations where blade 1 encounters the vortices generated by blade 2. The scales are in meters.

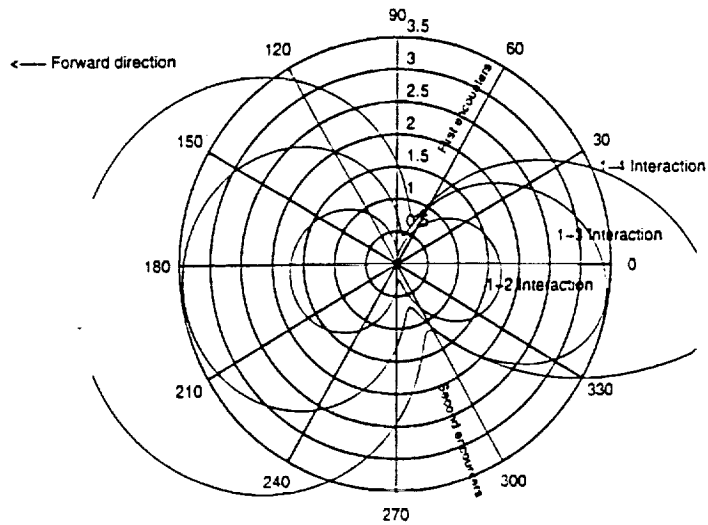


Figure 2.3: Polar plot of $d(t_n)$ vs θ for the different cases of blade 1 interacting with the vortices of blade 2, 3 and 4. The possible BVI source locations correspond to the notches where $d(t_n)$ is minimal. The first encounters occur at the blade advancing side, and the second encounters take place at the blade retreating side. The radial scale is the distance (meters) between the tip of blade 1 and the vortex that is encountered

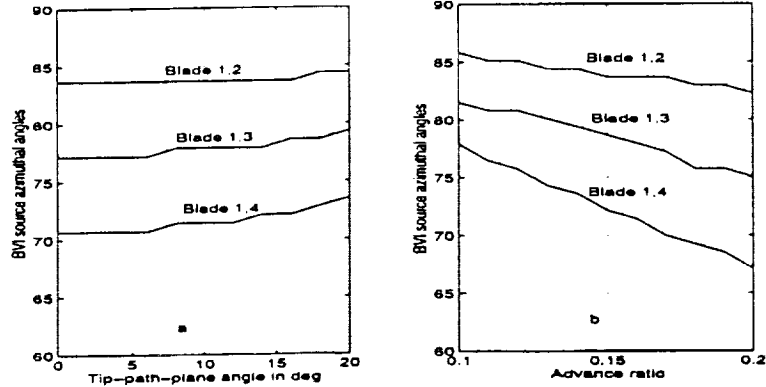


Figure 2.4: a. Source location azimuth angle vs tip-path-plane angle α for fixed advance ratio μ and descending rate V_d ; b. Source location azimuth angle vs advance ratio for fixed rotor RPM and tip-path-plane angle α .

90 degree location as the advance ratio increases. Figure 2.4 indicates that the BVI source locations are quite sensitive to the change of advance ratio. This result is in agreement with most experimental observations. The higher the advance ratio, the earlier the BVI encounters (the smaller the encounter azimuth angles) [9]. However, Figure 2.4 indicates the BVI source locations are not sensitive to the change of tip-path-plane angle. This is apparently not in agreement with the experimental observations [9], where the BVI source locations were found to be highly dependent on the tip-path-plane angle. The discrepancy likely arises from the simplicity of the model. In Figure 2.4 although the tip-path-plane angle is varied from 0 deg to 20 deg, the advance ratio, rotor RPM and descent rate are held constant. In real cases, however, the change of tip-path-plane angle will inevitably result in changes of rotor RPM, forward speed (or advance ratio) and descent rate. The simple model developed here is not able to account for the intricate aerodynamic and mechanical relations between all these parameters.

Figure 2.4 also indicates the time order of the occurrence of BVI encounters for the different pairs of blades. Obviously, blade 1 interacts with the vortex shed by blade 4 first (at an angle of around 70 deg), then blade 1 encounters the vortex shed by blade 3 (at an angle of 77 deg), and finally it encounters the vortex shed by blade 2 (at an angle of 84 deg). For the rotor speed of 300 RPM, the time delay between the first and second encounters is about 4 ms and the time delay between encounters 2 and 3 is the same. This is in agreement with actual data presented in Figure 2.5, where one BVI event is shown. This BVI event is obtained from averaging the in-flight test data of flight condition 39_24. Details of averaging are illustrated in the next Chapter. In Figure 2.5, the BVI event is composed of three spikes. The time delay between spike 1 and spike 2 is about 4 ms (with a rotor RPM of 300). Spike 1 (the highest and also the earliest spike) is a result of the interaction of blade 1 with the vortex of blade 4 since this BVI interaction occurs before the other two BVI interactions according to Figure 2.4. The event's size may be related to the fact that the vortex requires a certain amount of time to evolve into proper size for a maximum BVI event. Note that vortex 4 is the oldest of the set of three. The next oldest is vortex 3 and vortex 2 is the youngest of the three.

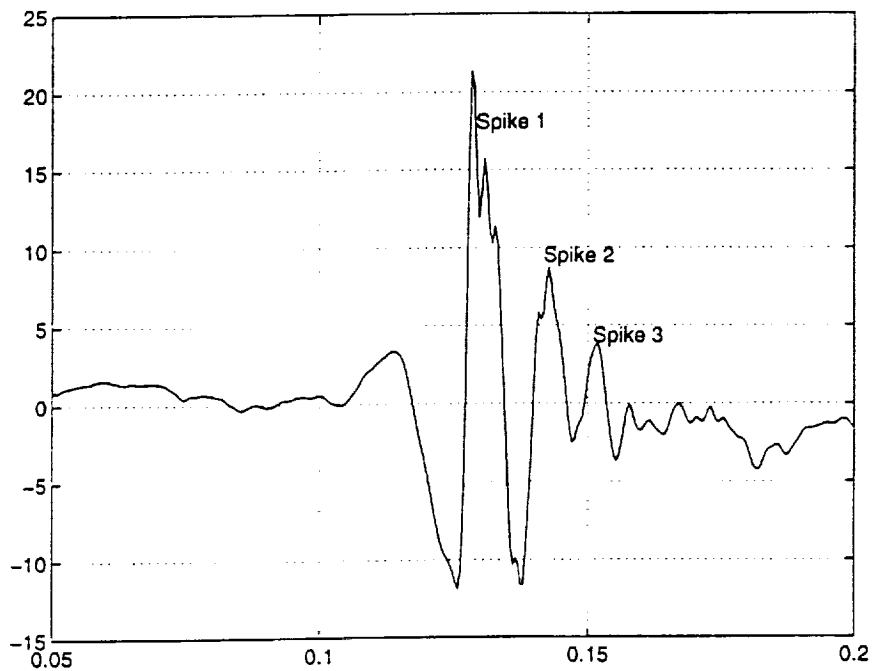


Figure 2.5: A typical BVI event composed of three spikes. Each spike corresponds to one interaction of one blade with the vortex shed downward by another blade. Comparing the time order of the three spikes with the time order of the BVI interactions in Figure 2.4 indicates that spike 1 (earliest and highest spike) is a result of blade 1 interacting with the vortex of blade 4. The next two spikes result from blade 1 interacting first with the vortex of blade 3 and then with that of blade 2.

2.4 BVI Noise Radiation Direction

2.4.1 Lateral directivity BVI noise

This report is only concerned with the BVI noise at the blade advancing side. Physical intuition suggests that, in the rotor plane, the BVI radiation direction is perpendicular to the blade span when the blade interacts with the vortex. Previous research and measurement results confirm this [7]. Figure 2.6 shows the the BVI radiation direction in the rotor plane. As clearly shown in Figure 2.6, the blade interacts with the vortex at an azimuth angle of

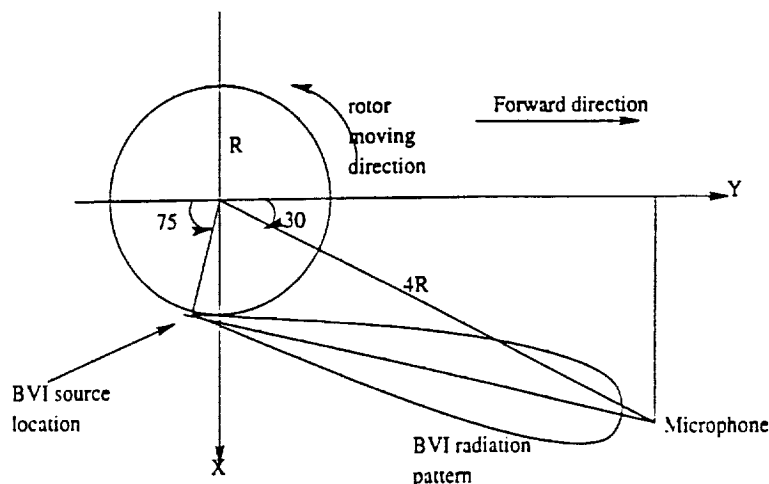


Figure 2.6: BVI radiation direction in the rotor plane. The microphone location is the same as reported in [5].

75° . This number should be comparable with Figure 2.4, where it can be seen that the BVI source locations range from 65° to 85° . A typical value is about 75° . Based on this value, the BVI radiation direction is then tangent to the rotor tip circle at an azimuth angle of 75° . In measurements reported by *Yamauchi et al* [5], a recording microphone was placed at a distance of four blade lengths ($4R$) away from the rotor center as seen in Figure 2.6. At this location, the center of the radiation lobe forms a 30° angle with the Y -axis. These numbers are comparable to the parameters used by *Yamauchi et al* [5] when performing the in-flight test and wind tunnel test. This comparability is discussed in later sections.

2.4.2 Longitudinal direction of BVI noise

Figure 2.7 shows BVI radiation in the side view plane. The acoustic source is the location very close to the leading edge of the rotor blade [8]. Detailed analysis of the exact geometry of the blade surface (airfoil) is beyond the scope of this report. The angle of 25° is taken from *Yamauchi et al* [5]. Notice that Figure 2.7 shows an upward radiation lobe in addition to the familiar downward radiation lobe. This upward radiation lobe has not been reported in the references examined. Assuming there is a comparable amount of radiation in the

lobe above the rotor plane, then this feature can be identified as the cause for the negative impulses observed in the wind tunnel data. This issue is discussed in later sections.

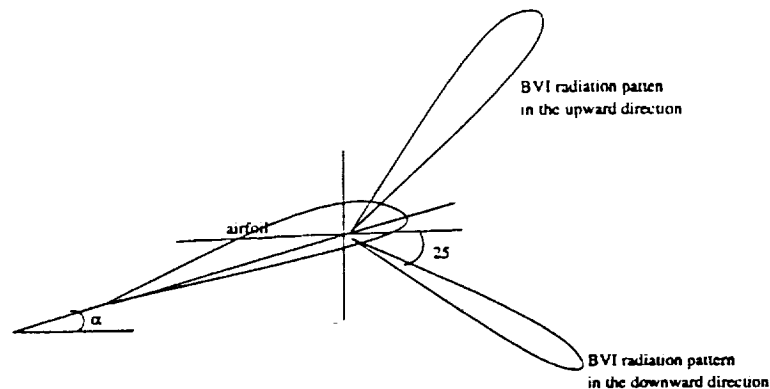


Figure 2.7: Longitudinal BVI radiation directivity.

2.4.3 Microphone location for maximum BVI

This section examines the 'ideal' microphone location for maximizing the BVI noise while minimizing the high-speed impulsive noise (for a typical BVI interaction azimuth angle of 75 deg). The principle is to put the microphone at the center of the BVI radiation lobe. Based on the direction information provided in Figure 2.6 and Figure 2.7, we notice that the ideal location for the microphone is in the forward down direction with an azimuth angle of 150 deg and polar angle of 25 deg down from the rotor plane. The distance between the center of the rotor and the rotor plane projection of the microphone location should be $4R$ because this is the point where the radiation lobe center intersects the radial direction (from the rotor center) at an azimuth angle of 150 deg as shown in Figure 2.6. The direct distance between the rotor center and the microphone is therefore $4R/\cos(25)$, which is about 97 ft. -In *Yamauchi's* report, this direct distance between the microphone and the rotor center was set to be 88 ft ($4R$), and the rotor plane distance is $88 * \cos(25) \approx 80\text{ft}$ which falls 8' short of the ideal location as shown in Figure 2.8. The analysis here presumes the BVI noise comes from the blade tip, not from the rotor center. However, as stated earlier, BVI locations are commonly at distances of 0.6 to 0.8 R from the rotor hub. So although their microphone location is on the correct radial direction from the rotor center, it is apparently not at the center of the BVI radiation lobe that originates from the blade tip located at distance R from the rotor center and at an azimuth angle of 75 deg. The microphone location coordinates for these calculations (using their coordinate system) are shown in Figure 2.8. The microphone location for maximizing the direct BVI signals will vary for different flight configurations and this should be carefully taken into account in order to optimize the wind tunnel measurement environment. Also, it is seen in later sections that wind tunnel geometry and accurate estimates of the background noise play key roles in the data analysis necessary to extract the best BVI signal estimate from the data recorded in the wind tunnel.

⑥ A more correct microphone location (97°, -44°, 5.8')

⑥ Yamauchi's microphone location (83°, -40°, 5.8')

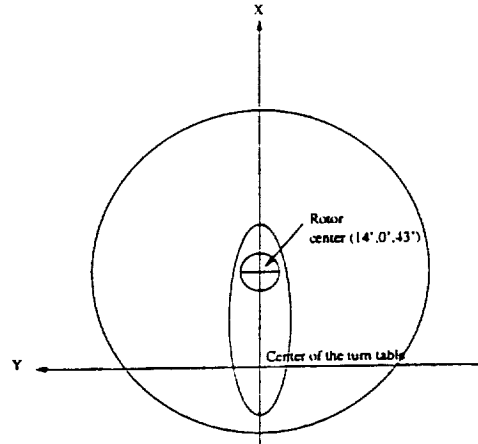


Figure 2.8: Microphone location for measuring the BVI noise vs the microphone location that's been actually used. The coordinate system of *Yamauchi et al* [5] is used here for easy comparison.

2.5 BVI waveform features

As illustrated in previous sections, although the vortices are continuously generated by the leading blades, the encounter between the trailing blades and the vortices only occur at certain discrete locations. Each encounter produces an impulsive sharp increase of pressure at the bottom of the blade. Therefore, in the down forward direction, each BVI encounter results in a corresponding positive spike (compressional acoustic wave). The width of the spike depends on the core size of the vortex and the tip velocity of the blade. The magnitude of the spike is related to the vortex strength and the blade attack angle. The model developed in the previous sections suggest that there are at least three BVI encounters at the advancing side, which implies that there are at least three spikes for each BVI event (due to one blade). The time difference between the spikes is the same as the time delay between each individual BVI encounter. The time delay has been calculated to be about 4 ms using the parameters from *Yamauchi's* flight 203. All these agree very well with the observed in-flight data as will be shown in later chapters.

It's worthwhile to emphasize the BVI upward radiation as this will cause special problems for wind tunnel measurement due to the reflections on the ceiling. The BVI noise in the upward direction is composed of negative spikes as shown in Figure 2.9. The reason is that the vortex increases the pressure at the lower surface of the blade, but reduces the pressure at the upper surface of the blade. Therefore, the radiation in the upward direction has opposite polarity as the downward radiation (dilatational acoustic wave, instead of compressional wave).

More mathematical justification of this statement can be found in [4], although *Schmitz and Yu* did not mention the radiation in the upward direction, their observed data suggest that the positive BVI spike decreases in magnitude and then changes polarity as the polar angle goes from 90 deg to 0 deg. This upward radiation is believed to be the cause of the numerous negative spikes observed in the wind tunnel test data provided by *Yamauchi et al* [5] and they will be discussed more in later chapters. The time delay between the direct path and the ceiling reflection path is about 45 ms, which agrees with the real data.

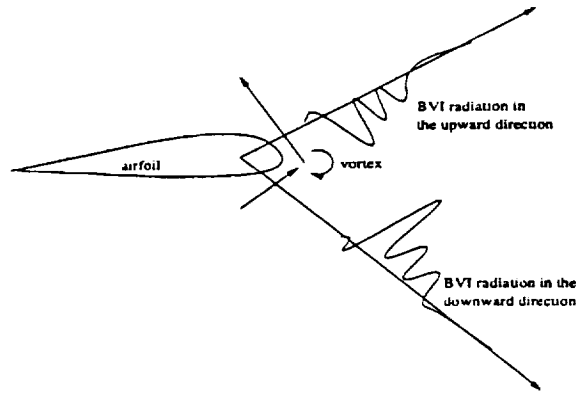


Figure 2.9: Longitudinal BVI radiation directivity.

2.6 Synthetic BVI events

Using the BVI locations determined in previous sections and the parameters similar to those in [5], the synthetic BVI events for flight condition 203 are computed and shown in Figure 2.10.

In Figure 2.10, forward speed and descending rate of flight 203 in [5] were used, but the rotor RPM was set at 300. Three BVI encounters at the advancing side were considered. The specific BVI source locations in terms of azimuth angles are 70.19 deg (blade 1 tip interacts with the vortex of blade 4), 76.98 deg (blade 1 with blade 3) and 83.77 deg (blade 1 with blade 2). The time delay between the first interaction and the second interaction is 3.9 ms. The time delay between the second and third encounters is the same. This time delay is seen as the time delay between the BVI positive spikes as clearly shown in part b of Figure 2.10. The individual 'wavelet' generated by each BVI encounter is modeled by the following function:

$$s(t) = [1 - 4(\sigma t)^2 + \frac{4}{3}(\sigma t)^4]e^{-(\sigma t)^2} \quad (2.6)$$

This seemingly odd-looking function is nothing but the normalized fourth degree derivative of a Gaussian function. It was selected because its shape qualitatively matches the measured data. Figure 2.11 displays the basic wavelet represented by the function.

Also, it will be seen in a later section that this function serves well in constructing a composite BVI waveform which includes direct and reflected contributions in the wind

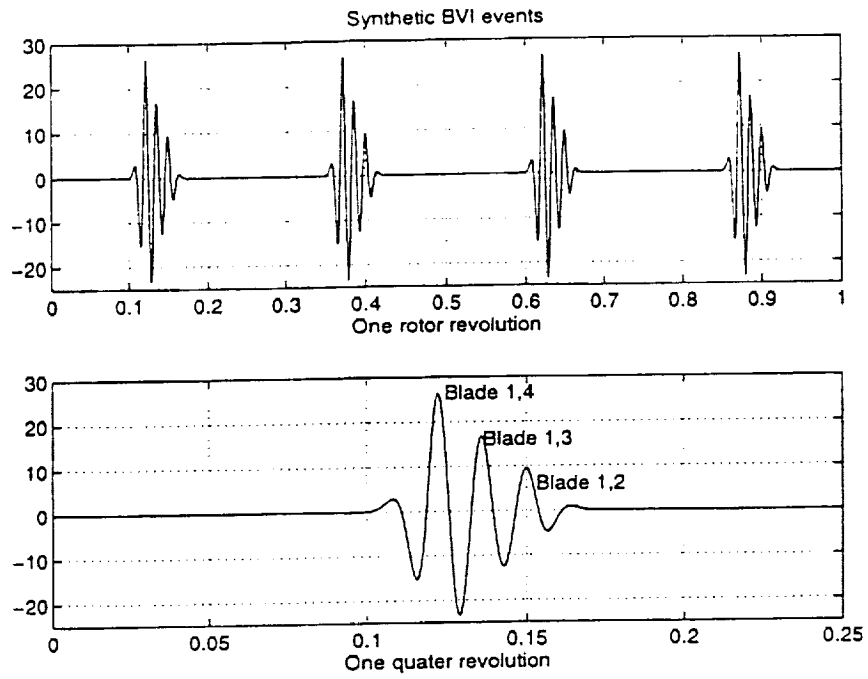


Figure 2.10: Synthetic BVI events for the in-flight condition 203.

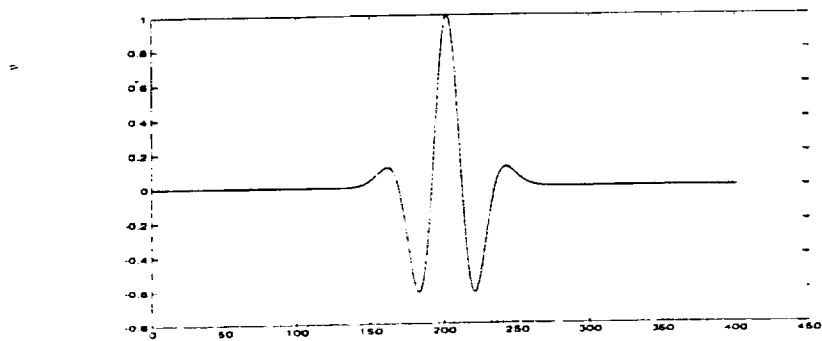


Figure 2.11: Wavelet used to construct synthetic BVI signals.

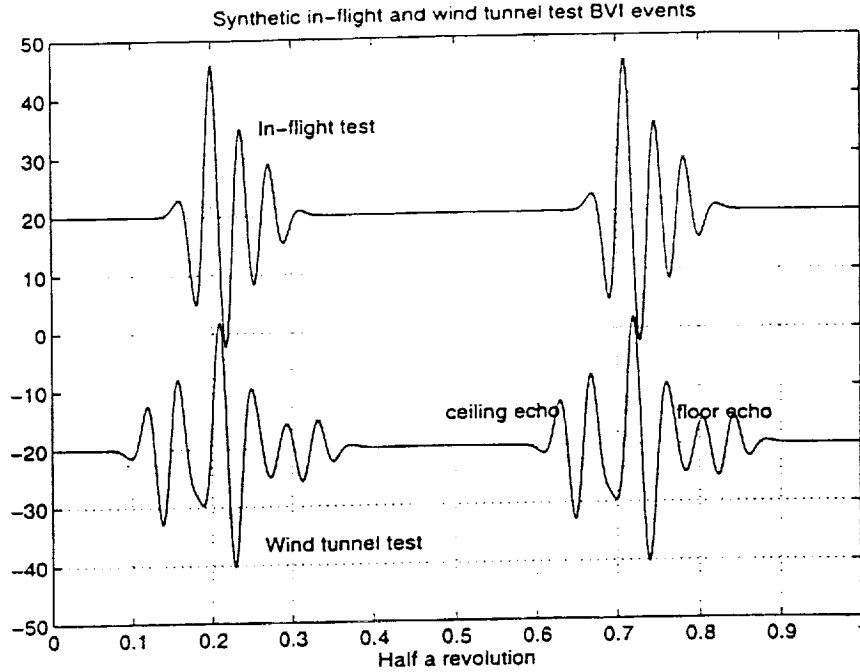


Figure 2.12: Synthetic BVI events for the in-flight condition 203 compared with synthetic wind tunnel BVI signals.

tunnel. The width of the spike can be adjusted by varying the parameter σ . In Figure 2.10, for example, $\sigma\delta t = 0.7$, where δt is the sampling time interval. The BVI events in Figure 2.10 are formed by convolving this wavelet with three impulses that represent the BVI encounter times and strengths:

$$s = \underbrace{[0, \dots, 0, 25, 0, \dots, 0, 13, 0, \dots, 0, 8, 0, \dots, 0, 25, 0, \dots, 0, 13, 0, \dots, 0, 8, 0, \dots]}_{512} \quad (2.7)$$

where the numbers indicating the BVI strength (25, 13, 8) are set according to the averaged flight 203 flight data (as explained in later chapters). A sample rate of 10012 sps is used in the above equation (the same as in *Yamauchi's* report and one blade revolution corresponds to 2048 data points. Therefore, one quarter revolution corresponds to 512 samples and the sample delay between the individual BVI encounters is 40 samples (equivalent to 3.9 ms in time).

Figure 2.12 shows the synthetic BVI events inside a wind tunnel. The flight condition is the same as in Figure 2.10 (flight 203 in [5]), except that the 'flight' is carried out inside the wind tunnel. For comparison, the synthetic in-flight BVI events are also plotted along with the wind tunnel BVI events.

The BVI events in Figure 2.12 are formed by convolving the synthetic BVI events in Figure 2.10 with the chain of reflection coefficients that represent the reflections at the floor

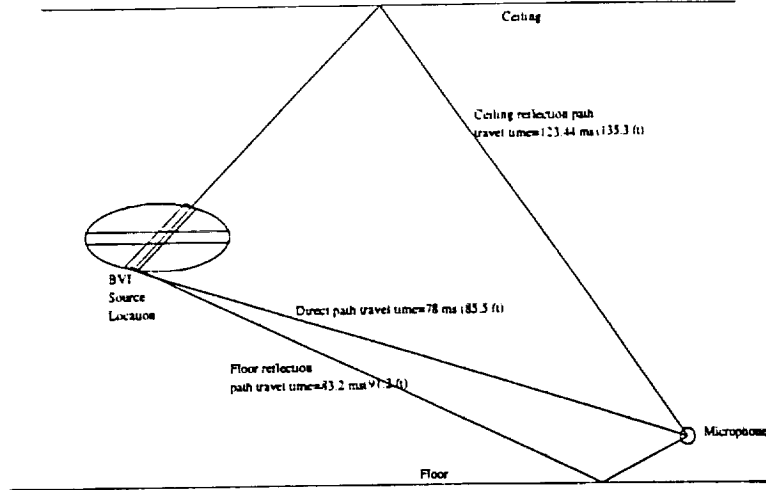


Figure 2.13: Geometry of the wave propagation paths inside the wind tunnel

and on the ceiling respectively:

$$r = [1, \underbrace{0, \dots, 0}_{52}, 0.5, 0, \dots, 0, -0.5] \quad (2.8)$$

450

where the number '1' represents the direct path BVI event, '0.5' represents the reflection coefficient at the floor [5] and '-0.5' is the reflection at the ceiling. The real physical reflection coefficient on the ceiling should be positive. The negative sign comes from the fact that the upward radiation has opposite polarity as the downward radiation. This is equivalent to setting the ceiling reflection coefficient to a negative number. The sample delay of 52 corresponds to the time delay between the direct path and the floor reflection path as shown in Figure 2.13 (5.2 ms). Likewise, the sample delay of 450 represents the time delay between the direct path and the ceiling reflection path (45 ms). The detailed geometry of the various acoustic wave propagation paths are shown in Figure 2.13. Multiple reflection effects are ignored here. Strictly speaking, the air flow through the tunnel makes the medium equivalent to an anisotropic medium, and the propagation path is no longer a straight line as in Figure 2.13. But for slow flight speed, the apparent wind speed is less than one tenth of the sound speed, and therefore, the wind effect on the propagation path is negligible.

2.7 Comparison of synthetic and real BVI events

To verify the appropriateness of the model developed here, we compare the synthetic BVI events with the real measurement. Figure 2.14 shows the comparison for in-flight test 203. In Figure 2.14, the synthetic BVI events were created in the same way as in Figure 2.10. The real data in Figure 2.14 is the result of averaging the whole data set of flight 203 as will be shown in the next chapter. Simple visual examination suggests that the synthetic events captured the essential features of the observed BVI impulsive noise.

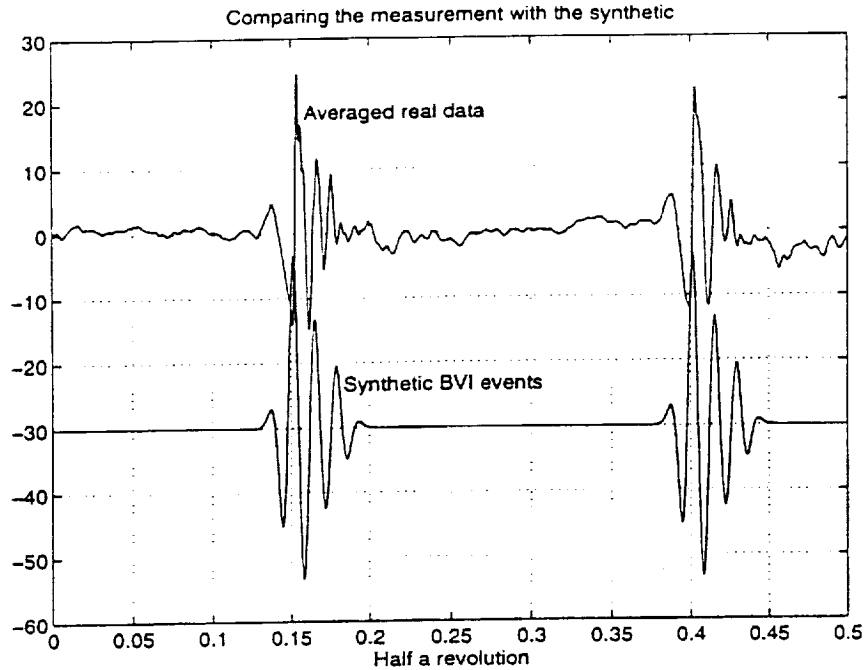


Figure 2.14: Compare the synthetic BVI events with the real measurement for in-flight test 203

Figure 2.15 shows the comparison between the synthetic BVI events and the real measurement for the wind tunnel test 39.24 [5]. Again, the process of obtaining the synthetic BVI events is the same as in Figure 2.12. The real data sequence is a result of averaging and filtering (remove the background noise) the measured results of 39.24. Details of the processing procedures will be illustrated in Chapter 4. As is clear in Figure 2.15, the essential features of the BVI impulse noise inside a wind tunnel has been captured by the synthetic data. For instance, before the major BVI event, there are signals that originate from the reflection on the ceiling. Following the major BVI events, there are more smaller spikes that originate from the reflection on the floor. The exact waveform of the reflected fields are different from the observed data. The complicated appearance of the reflected spikes might be caused by the dispersive nature of the acoustic material (lining) that covers the floor and the ceiling.

2.8 Effect of changing wind tunnel measurement geometry

The multipath signals inside the wind tunnel create a complex waveform which obscures the desired direct BVI signal. Figure 2.16 shows the contributions to the synthetic BVI waveform inside the wind tunnel. Both the ceiling reflection and the floor reflection events overlap the inflight (direct) BVI event. Since the time for 1/4 revolution is 50 ms and the ceiling reflection delay is 45 ms, the ceiling reflection shown is from the previous BVI event

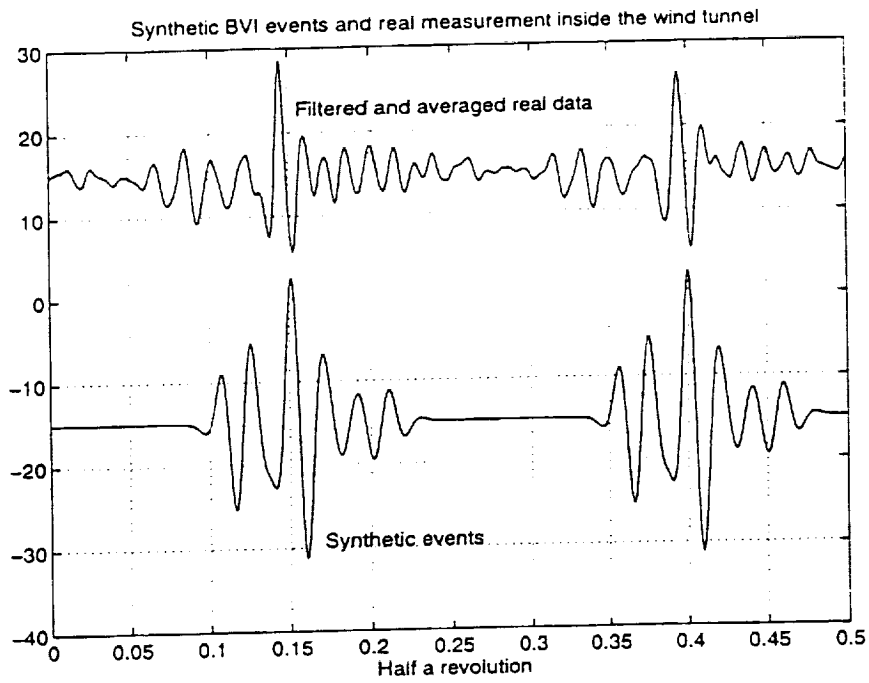
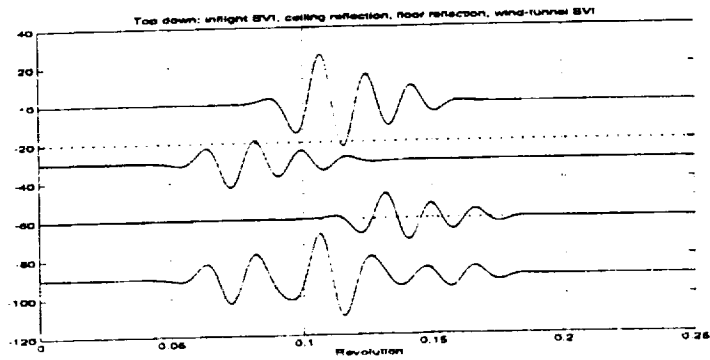


Figure 2.15: Comparing the synthetic BVI events with the real measurement for wind tunnel test 39_24



*make larger
like 2.17
perhaps*

Figure 2.16: Multipath constituents contributing to the synthetic wind tunnel signal

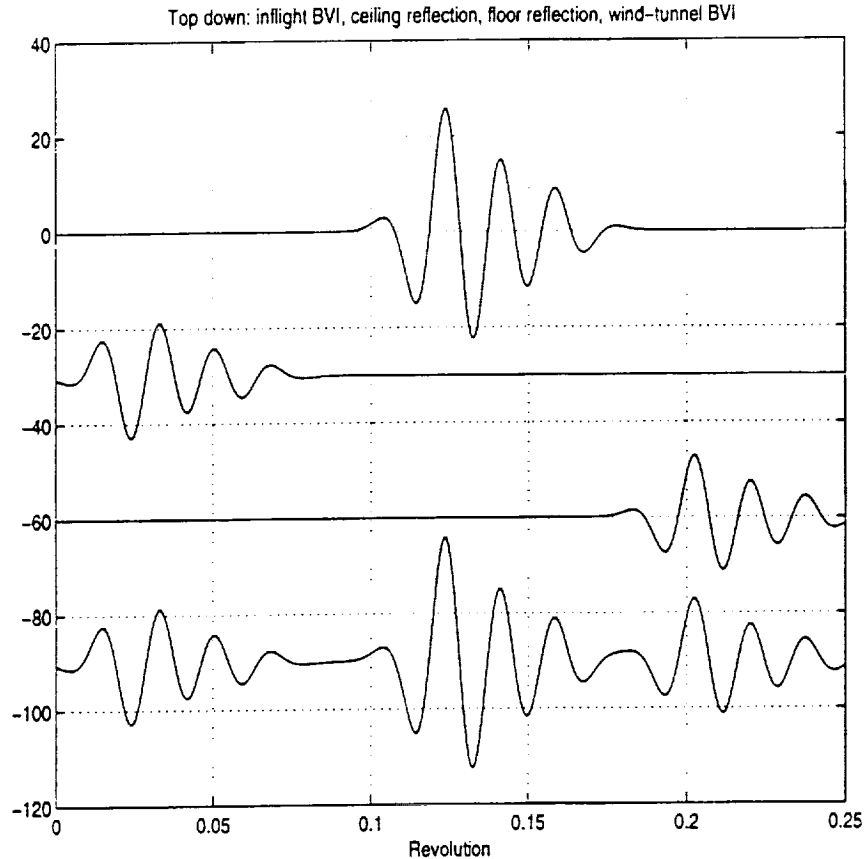


Figure 2.17: Synthetic BVI event produced with both rotor hub and microphone raised by 10 feet

in the wind tunnel. However, the floor event shown in Figure 2.16 is from the current BVI event. The relative positions of the multipath signals to the direct signal can be changed by changing the measurement geometry. Raising both the rotor hub and the microphone aids in signal separation since this action shortens the ceiling delay time (moves the ceiling event forward in time toward its BVI event in the previous 1/4 revolution) and lengthens the floor delay time (moves the floor event to later time away from its BVI source event). Figure 2.17 shows the effect of raising both the rotor hub and the microphone a distance of 10 feet while leaving the xy coordinates unchanged. There is a clear separation of the ceiling event from the desired BVI event and the floor event is almost separated as well. Moving the rotor and microphone up the same distance has the advantage of preserving the downward angle to the microphone from the rotor plane. Consequently, the microphone remains in the direction of maximum BVI signal radiation.

Figure 2.17 shows there is benefit in changing the measurement geometry in the wind tunnel. Another change one might consider is moving the microphone directly along the line from the rotor hub to the microphone. The effect of these changes has not been considered for this report and is left for later consideration.

Chapter 3

BVI Feature Extraction by Time-domain Averaging

3.1 Introduction

One of the important tasks of this research is to extract the essential BVI signal features (waveforms) from the measured data of many revolutions. After the BVI waveforms are obtained, it is then possible to further analyze the dependence of the BVI signal on some of the flight condition parameters such as advance ratio, tip-path-plane angle and descent rate etc. The difference between the BVI event associated with each individual blade will also become clear. Comparisons between the averaged in-flight test data and the averaged wind tunnel test data obtained under similar flight conditions will illustrate the feasibility of using the wind tunnel as a way to measure the BVI signal. The simplest, and probably also the most effective way to extract the BVI waveform is by time-domain averaging. The measured BVI data from different rotor revolutions contains some random variations that we attribute to any acoustic emissions other than the BVI radiation. By averaging, we hope to remove the random variations but keep the essential BVI waveforms unaltered.

The critical averaging issue is finding a proper way to align the data segments from different revolutions. Without proper alignment, averaging will smear the sharp impulsive nature of the BVI waveform. In the following sections, issues of alignment, averaging and analysis of the BVI waveforms are presented.

3.2 Data alignment for the in-flight test results

3.2.1 Preliminary visual examination of the data

NASA-Ames provided three sets of in-flight test data collected under three different flight conditions. A schematic diagram of the flight formation used for collecting the in-flight test data is shown in Figure 3.1. The microphone was placed on the tail of the leading YO-3A airplane. On the plan view, the airplane was flying at the right forward side of the S-76 C helicopter with an azimuthal angle of $\Phi = 30^\circ$ and a distance of 88 ft. On the side view, the YO-3A airplane was flying in the forward down direction with an angle of 25° . A More

detailed description of the flight formation can be found in [5].

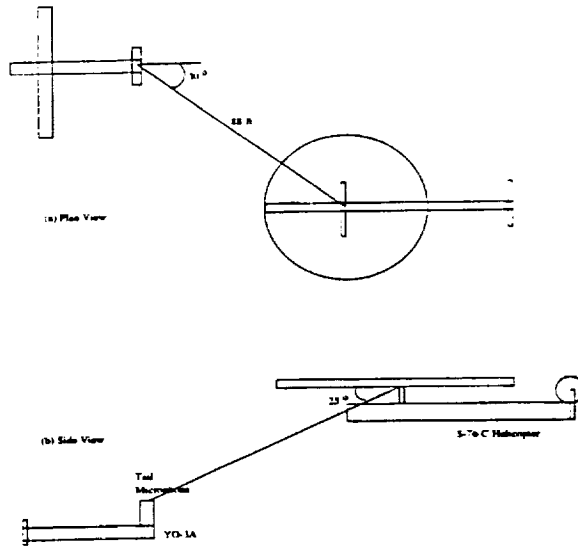


Figure 3.1: Flight formation used during the in-flight test

Figure 3.2 shows an example of the BVI data for condition 203 [5]. It is a short segment of the original data set with only three revolutions. Notice that each revolution consists of four BVI events (waveforms) since the tested helicopter is four-bladed. The original data set from NASA-Ames contains up to 50 revolutions.

As is clear in the figure, the BVI waveforms from each revolution are quite different. Therefore, averaging is a logical way to obtain the 'essential' BVI waveforms while minimizing the random variations. If the time interval of each revolution is the same, then we can simply perform the averaging across each revolution. But the real situation is not that simple. According to [5], the data sampling rate was so chosen that each revolution contains 2048 data samples. If we take this number as true, and divide the whole data set into 50 segments with each segment having 2048 data points, then the mis-alignment problem caused by the non-constant time interval of each revolution becomes apparent as shown in Figure 3.3. Two segments of the data are shown from two arbitrary revolutions. The major BVI events are obviously not aligned properly. Simple averaging across these two revolutions will definitely harm the sharp impulsive signature of the BVI waveforms.

The conclusion from Figure 3.3 is that data-shifting and alignment using a fixed data length for each revolution does not work. A more sensible way is to align the data by using the BVI's impulsive features. Yamauchi [5] suggested aligning the data by the position of the major spike on each BVI event. This may work for condition 203 where the BVI signal is much stronger than the background noise. For the other two conditions, the BVI signal strength is much weaker and locating the position of the major BVI spike becomes problematic. As the results in the following sections will indicate, data alignment using some statistical criteria works better and the algorithm is more robust. The statistical criteria take into account the whole BVI event, not just the major spike. In addition, both Figure 3.2 and 3.3 imply the existence of significant differences between the BVI event due to different

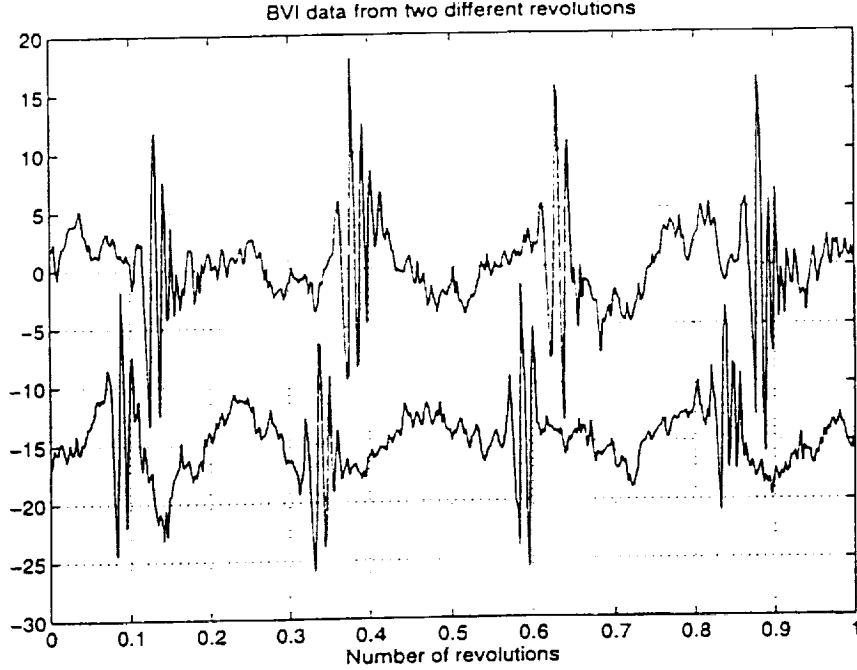


Figure 3.3: Plot of BVI data from two arbitrary revolutions of flight 203. Each revolution is assumed to have 2048 data samples. The major BVI events are not aligned, indicating that the real time interval of each revolution is different from the data length of 2048 data samples

is different. For the in-flight test, one likely cause of $\Delta T_i(m)$ is the slight change of distance between the test helicopter and the YO-3A airplane that carries the microphone at its tail. $\Delta S_i^m(n)$ represents the random non-BVI acoustic noise embedded in the BVI signals. This is the term we want to average out and it is also defined in the range of $0 < n < T/4$. The basic assumption implied behind the averaging algorithm is that the random acoustic noise $\Delta S_i^m(n)$ at each different revolution is uncorrelated and has a mean value of zero. That is to say:

$$\lim_{M \rightarrow \infty} \frac{1}{M} \sum_{m=0}^{M-1} \Delta S_i^m(n) = 0 \quad (3.3)$$

for all $0 < n < T/4$ and $i = 1, 2, 3, 4$.

In this research report, data alignment was performed on the BVI signal due to each individual blade in different rotor revolutions. We use the BVI signal due to the first blade $S_1(n)$ as an example to illustrate the alignment procedures.

First we assign the BVI signal of the first blade ($i = 1$) in the first rotor revolution ($m = 0$) as a reference signal $x(n)$. That is:

$$x(n) = S_1[n - \Delta T_1(0)] + \Delta S_1^0(n) \quad (3.4)$$

Designate the BVI signal of the first blade ($i = 1$) in $(p + 1)$ th rotor revolution as $y(n)$. That

is:

$$y(n) = S_1[n - pT - \Delta T_1(p)] + \Delta S_1^p[n - pT - \Delta T_1(p)] \quad (3.5)$$

Now we want to align the signals $x(n)$ and $y(n)$. First we should shift $y(n)$ to the left by the amount of pT to obtain:

$$y'(n) = y(n + pT) = S_1[n - \Delta T_1(p)] + \Delta S_1^p[n - \Delta T_1(p)] \quad (3.6)$$

To do this requires the estimation of T , which can be regarded as a rough estimate of the mean value of the rotor revolution period. For the in-flight test data, T can be assigned to the value of 2048. But for the wind tunnel test data, T must be estimated from the auto-correlation of the original data set. After obtaining $y'(n)$, the next task is to further shift $y'(n)$ in a finer scale so as to move out the time difference $K = \Delta T_1(0) - \Delta T_1(p)$. To find this K value, two methods can be used, which originate from two different ways of measuring the similarity between two multi-dimensional vectors (the two signals $x(n)$ and $y'(n)$ can be regarded as two $T/4$ dimensional vectors). The first method is to find the K value so that the inner product (cross-correlation) of the two signal vectors is maximal:

$$K = \underset{k}{\operatorname{argmax}} \sum_{n=1}^{T/4} x(n)y'(n+k) \quad (3.7)$$

Another method is to find the K value such that the Euclidean distance between the signal vectors is minimal:

$$K = \underset{k}{\operatorname{argmin}} \sum_{n=1}^{T/4} [x(n) - y'(n+k)]^2 \quad (3.8)$$

Both methods were applied to BVI data and the results indicate that the latter method performs better. To show this, an example of the data alignment procedure is shown in Figure 3.4. The figure shows two BVI signals due to the same blade but at different rotor revolutions. The top part (A) shows the signal after simple shifting of the integer multiples of the rotor period (after shifting by pT). The middle part (B) shows the results after further shifting based on the cross-correlation algorithm. It's obvious that the cross-correlation algorithm fails to correctly align the data in this case. The bottom part (C) shows the results after using the Euclidean distance algorithm. The figure clearly shows the correct alignment by this algorithm, which suggests that the latter method works better than the correlation based method.

After obtaining K , averaging can then be performed over these two data segments to obtain a better estimate of the essential BVI waveform:

$$S'_1(n) = [x(n) + y'(n+K)]/2 \quad (3.9)$$

Averaging over more data segments can be implemented in the same manner.

One may argue that a more accurate algorithm should take into account not only the time delay between the two BVI signals, but also the compressional or dilational effect of

Calculated from Figure 3.5

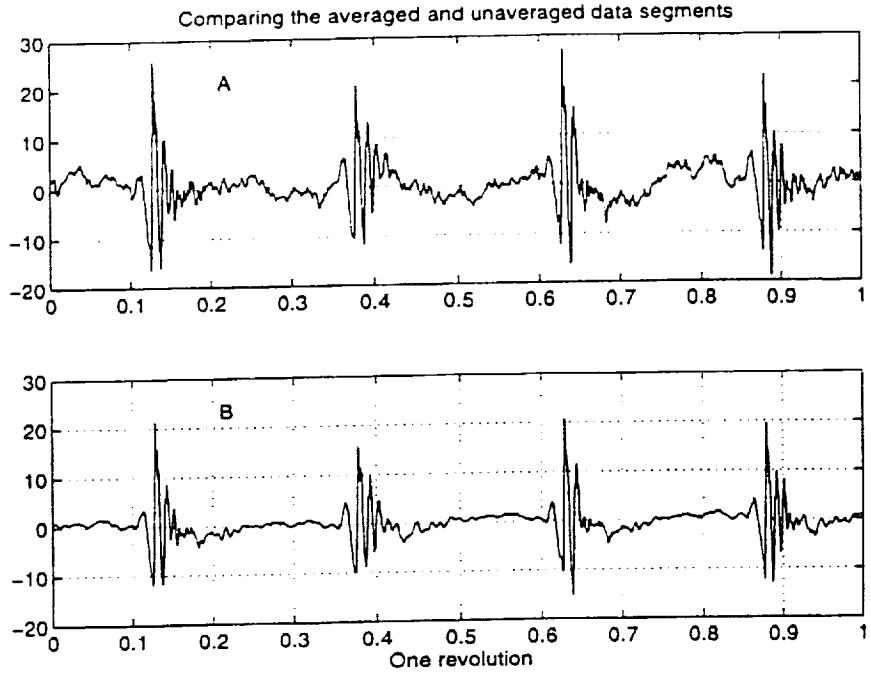


Figure 3.6: Compare the averaged BVI events with one of the unaveraged raw data segments for flight 203. A: Unaveraged raw data segment. B: Averaged data segment

major BVI events are greatly suppressed. There is no apparent smearing effect, indicating the correct alignment of the data was made before averaging. The magnitude of the major spikes are comparable before and after averaging. The most striking visual effect of averaging is that, after averaging, the four major BVI events become cleaner (free from high-frequency random variations) and are clearly separable from each other now. Before averaging, there is significant amount of signal energy between any two neighboring BVI events. After averaging, however, the signals between two major BVI events are quite small indicating averaging's effectiveness in enhancing the major impulsive BVI events while suppressing the non-BVI signals that lie between any two neighboring BVI events. Note too that individual BVI events are distinctly different.

3.2.4 Processed results for flight condition B: No. 307

The relevant flight condition parameters for this case are $V_D = 306 \text{ ft/min}$, $M_{tip} = 0.606$, $V_{true} = 82.7 \text{ Knots}$, $\mu = 0.203$, $\alpha = 0.1$. This case is known to produce the weakest BVI signals [5]. As a result, data alignment becomes more difficult due to the small signal-to-noise ratio. The data alignment results are shown in Figure 3.7. Procedures used in obtaining this figure are the same as in Figure 3.5. The curves corresponding to the four major BVI events on the raw data segments again indicate the random variations of the rotor revolution period that may be due to the distance variation between the YO-3A and the helicopter and due to the variation of rotor RPM. The performance of the data alignment

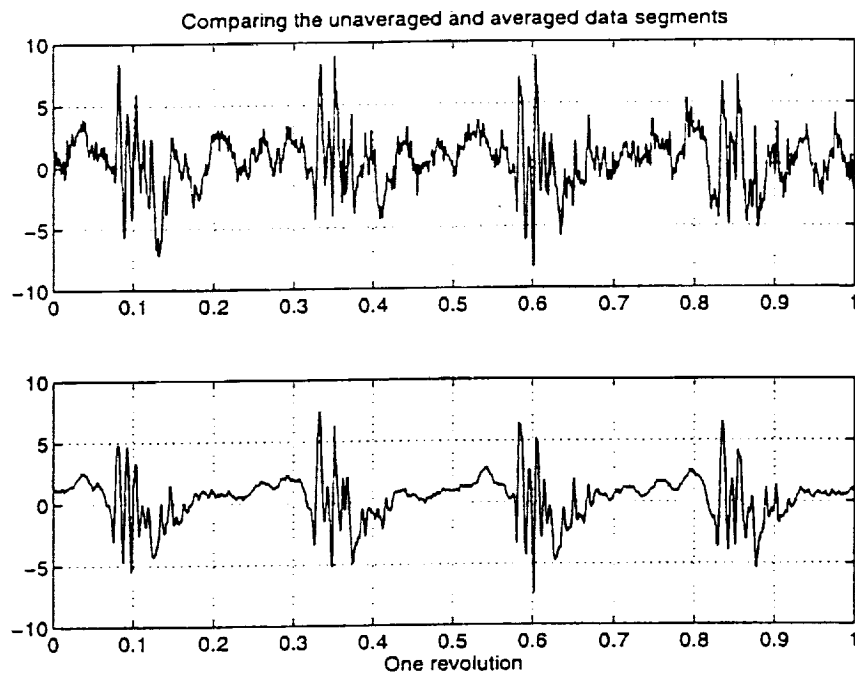


Figure 3.8: Compare the averaged BVI events with one raw data segment for flight 307. Top: Raw data segment. Bottom: Averaged data segment

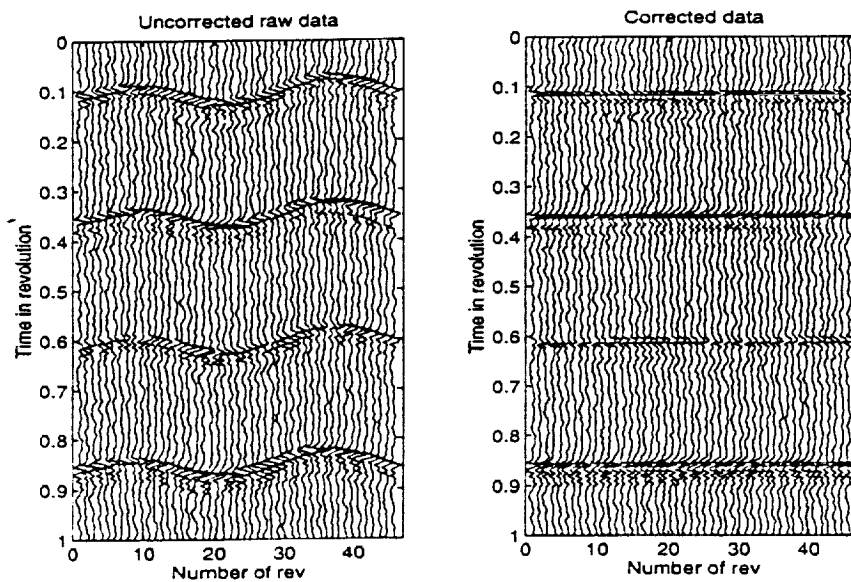


Figure 3.9: Plots of the unaligned and aligned data for flight 315. Left: Plot of the data after simple shifting of multiples of revolution period. Right: Plot of the data after further shifting using the Euclidean distance algorithm

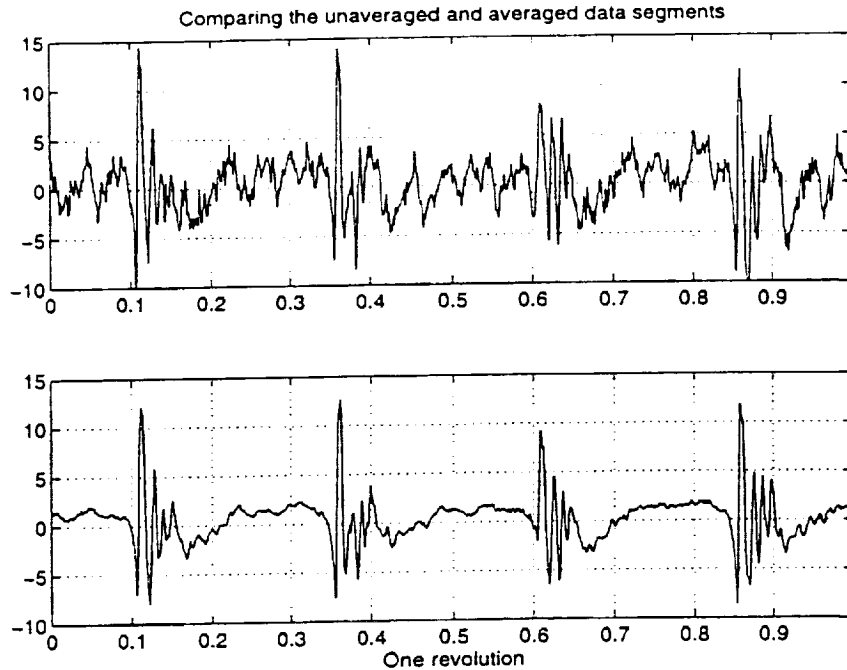


Figure 3.10: Comparing the averaged BVI events with one of the unaveraged raw data segments for flight 315. Top: Unaveraged raw data segment. Bottom: Averaged data segment

flight condition 307. Note again the individual BVI characteristics are different. Detailed comparison between the BVI waveforms from different flight conditions is presented in a later sections.

3.2.6 Comparison of the averaged BVI waveforms from different blades and at different flight conditions

Figure 3.11 shows all three averaged BVI data sets together. To illustrate the differences between the BVI waveforms due to different blades, the averaged data sets are 'circularly' shifted for better comparison. As clearly shown in the figure, the three data sets all indicate that the BVI signal caused by the first blade is weaker than the BVI signal due to the other three blades. The BVI signals due to the other three blades are rather similar and comparable. These records suggest that the first blade is different from the other three blades.

Comparing the three data sets at different flight conditions indicates that flight condition 203 generated the strongest BVI signals, whereas flight condition 307 produced the weakest BVI waveforms. Examining the flight parameters seems to suggest that the descent rate V_D is the crucial parameter that determines the intensity of the BVI signals. The higher the descent rate, the larger the BVI intensity. The other parameters, such as advance ratio μ and tip-path-plane angle α do not have a clear monotonic proportionality with the BVI intensities. Further comparison indicates that the BVI waveform signatures of flight 203

the audio produced from the in-flight tests and the wind tunnel tests also illustrates the presence of wind tunnel background noise. Background noise removal using optimal-filtering is discussed in the next chapter. Here we use averaging to reduce the background noise. Further examination of the data again shows the difference between the BVI events due to each individual blade, and there is visible difference between the signals from each rotor revolution.

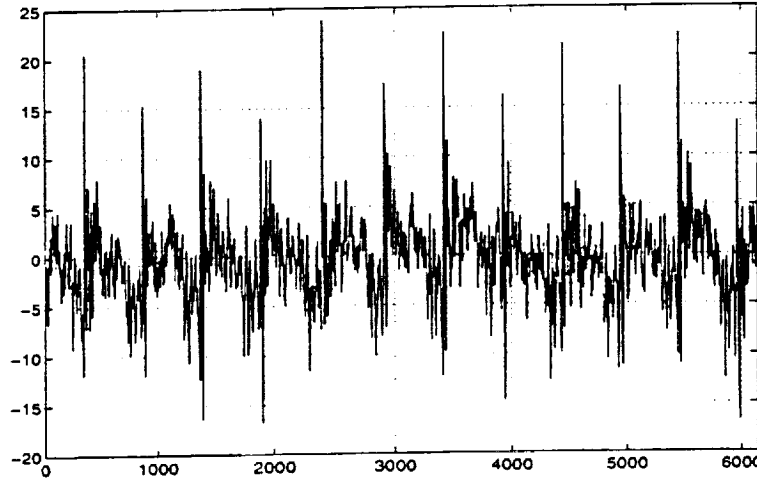


Figure 3.12: A short segment of wind tunnel test data of flight condition A 39_24 where $\mu = 0.173$, $\alpha = 5.1$ and $V_D = 741 \text{ ft}/\text{min}$. This condition is the nearest match to in-flight test 203. The data segment contains three revolutions and each revolution has four major BVI events

The averaging procedures used are the same as those used for averaging the in-flight test data except that in this case, the mean rotor revolution period was not assumed to be 2048 data samples. The period has been estimated from the real data by an auto-correlation scheme for each of three data sets and has been found to vary from 2032 data samples up to 2056 data samples. Using the estimated rotor revolution period, instead of a fixed 2048 data samples makes the data alignment more precise. The overall difficulty of aligning the wind tunnel data and then averaging the data is greater than that for the in-flight test data.

3.3.2 Processed results for flight condition A: No. 39_24

The relevant flight parameters for this case are shown in Figure 3.12. The data alignment results are shown in Figure 3.13. The left part of the figure is the result of time shifting by integer multiples of the estimated mean rotor revolution period. The non-horizontal but nearly straight four lines that correspond to the BVI events are vivid contrasts to the in-flight test results where the events are curved lines. This suggests that in the wind tunnel test, the distance between the BVI source location and the microphone location is fixed (a constant) and the rotor RPM was constant as well. This shows one advantage of the wind tunnel test. After further more precise alignment using the Euclidean distance algorithm,

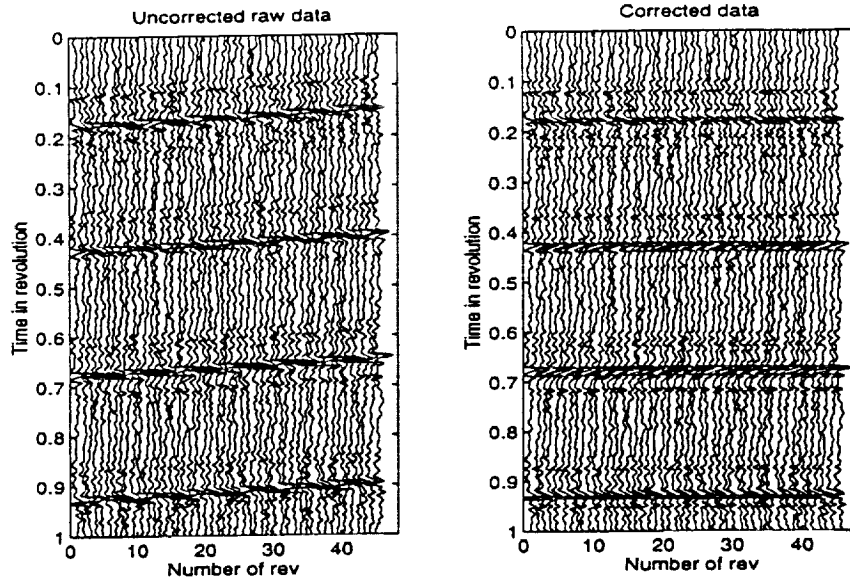


Figure 3.13: Plots of the unaligned and aligned data for wind tunnel test 39_24. Left: Plot of the data after simple shifting by multiples of the revolution period. Right: Plot of the data after further shifting using the Euclidean distance algorithm

the BVI events are completely aligned and become horizontal as shown in the right part of the figure.

After data alignment and averaging across each revolution, the comparison between the averaged BVI events and one of the unaveraged raw data segment is shown in Figure 3.14. The averaged result is excellent in terms of minimizing the non-BVI random variations, but enhancing or retaining the impulsive nature of the BVI waveforms. After averaging, the major BVI events become well separated and the wind tunnel background noise is quite successfully diminished by the averaging process. The difference between the BVI events due to each individual blade is less apparent in this case. There are several negative and positive small magnitude spikes preceding and following the major BVI events, which can be attributed to the ceiling and floor reflections as discussed in Chapter 2.

3.3.3 Processed results for flight condition B: No. 48_19

The relevant flight condition parameters are $V_D = 245 \text{ ft/min}$, $V_{true} = 79.9 \text{ kts}$, $\mu = 0.2$, $\alpha = 0$. This is the case known to produce the weakest BVI signals and is supposed to match the in-flight condition B 307. The low signal-to-noise ratio makes data-alignment more difficult and it is harder to judge the merit of averaging. The data alignment results are shown in Figure 3.15. The left part of the figure is the result of time shifting by integer multiples of the estimated mean rotor revolution period. The lines that correspond to the four BVI events are very nondistinct in this case, indicating that the intensity of the BVI signals is quite small, and all have almost the same level as the background noise. After alignment, the data are shown on the right of the figure. The data alignment appears to be successful in

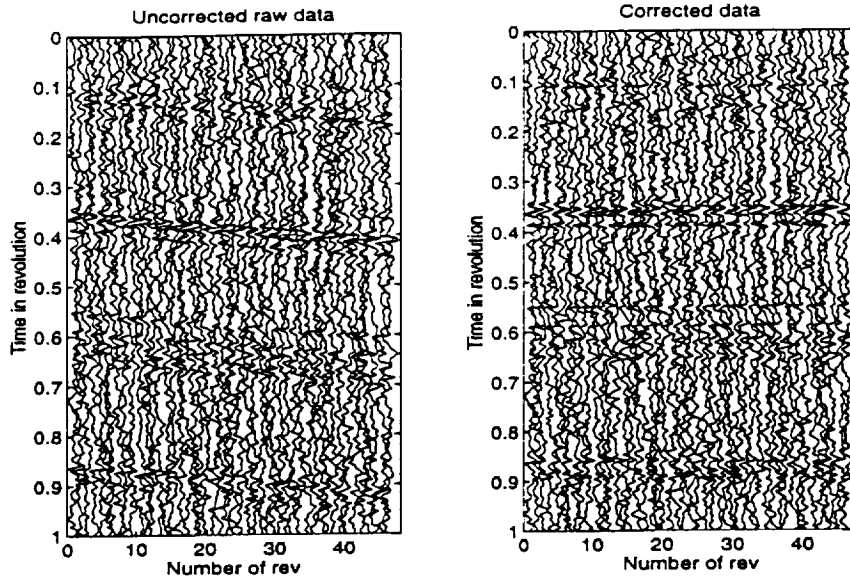


Figure 3.15: Plots of the unaligned and aligned data for wind tunnel test 48_19. Left: Plot of the data after simple shifting of multiples of revolution period. Right: Plot of the data after further shifting using the Euclidean distance algorithm

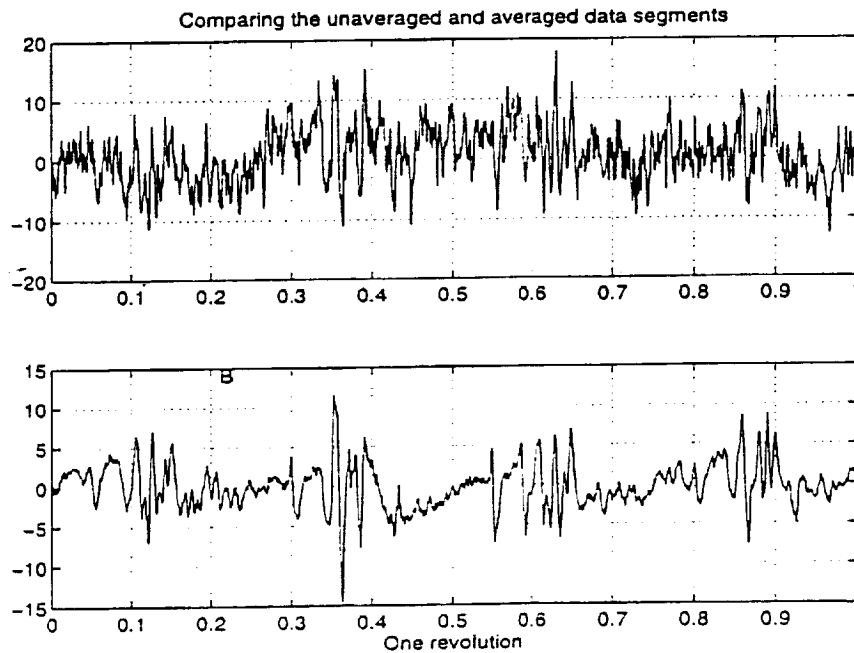


Figure 3.16: Comparing the averaged BVI events with one of the unaveraged raw data segments for wind tunnel 48_19. A: Unaveraged raw data segment. B: Averaged data segment

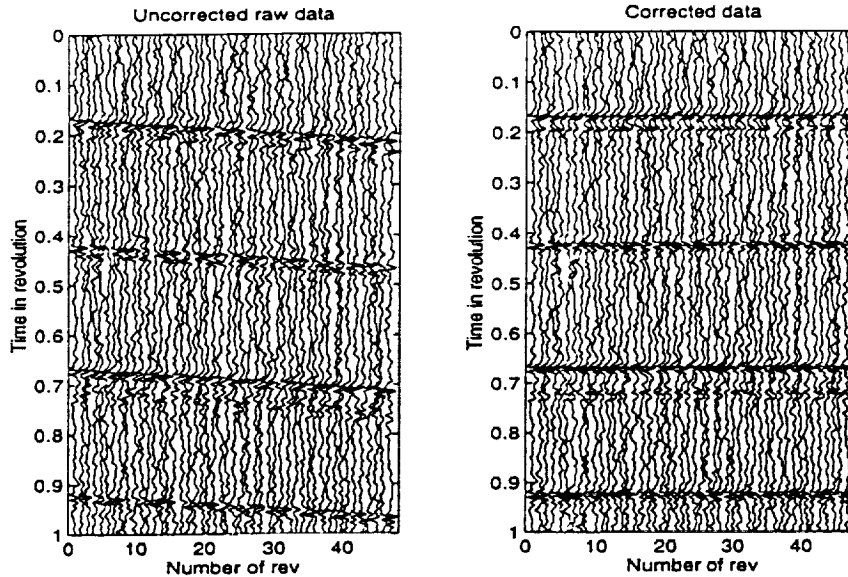


Figure 3.17: Plots of the unaligned and aligned data for wind tunnel test 48.18.
 Left: Plot of the data after simple shifting of multiples of revolution period.
 Right: Plot of the data after further shifting using the Euclidean distance algorithm

integer multiples of the estimated mean rotor revolution period. The non-horizontal but approximately straight four lines that correspond to the BVI events are evident. This suggests that in the wind tunnel test, the distance between the BVI source location and the microphone location is kept fixed (constant) and the rotor RPM was constant as well. After further more precise alignment using the Euclidean distance algorithm, the BVI events are completely level and become horizontal as shown in the right part of the figure.

After data alignment and averaging across each revolution, the comparison between the averaged BVI events and one unaveraged raw data segment is shown in Figure 3.18. The averaged result is good in terms of reducing the non-BVI random variations, but enhancing or retaining the impulsive nature of the BVI waveforms. After averaging, the major BVI events become well separated. The wind tunnel background noise are significantly reduced by the averaging process.

3.3.5 Comparison of the averaged BVI waveforms from different blades and at different wind tunnel flight conditions

Figure 3.19 shows all the three averaged BVI data sets. Again the averaged data sets are 'circularly' shifted for better comparison. Both case A and C indicate that the BVI signal due to the first blade is weaker than the signals produced by the other three blades. But the data from case B is less clear. The reason might be that this case has the weakest BVI signals and the averaging has not completely removed the background non-BVI noise. Also, the euclidian distance algorithm may be less successful in aligning the BVI events because of the poor signal to noise ratio in this data set.

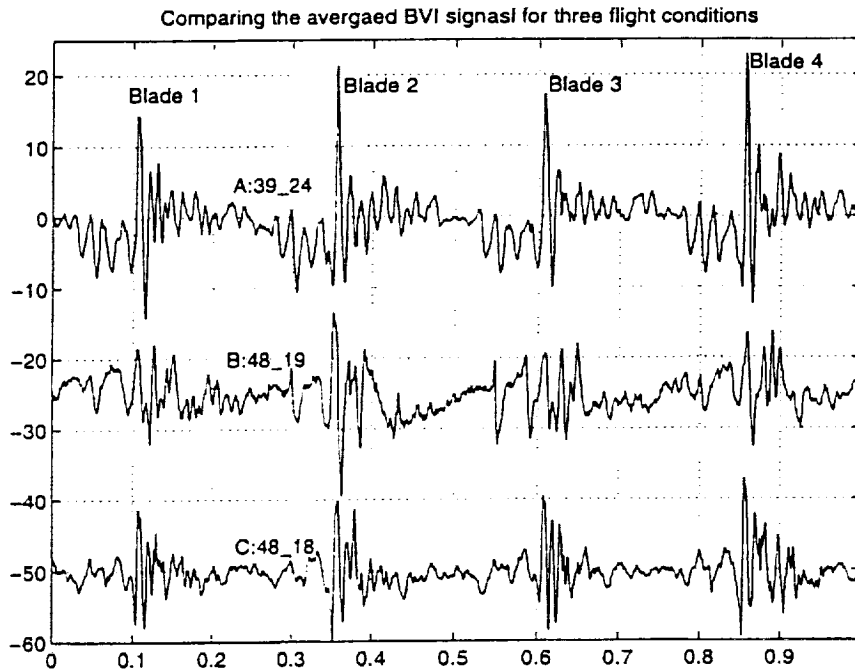


Figure 3.19: Comparing the averaged BVI waveforms from the three different flight conditions. Parameters for flight 39_24 are $V_D = 741\text{ft}/\text{min}$, $V_{true} = 69.8\text{kts}$, $\mu = 0.173$, $\alpha = 5.0\text{deg}$. Parameters for flight 48_19 are $V_D = 245\text{ft}/\text{min}$, $V_{true} = 79.9\text{kts}$, $\mu = 0.2$, $\alpha = 0\text{deg}$. Parameters for flight 48_18 are $V_D = 475\text{ft}/\text{min}$, $V_{true} = 100\text{kts}$, $\mu = 0.251$, $\alpha = 0\text{deg}$

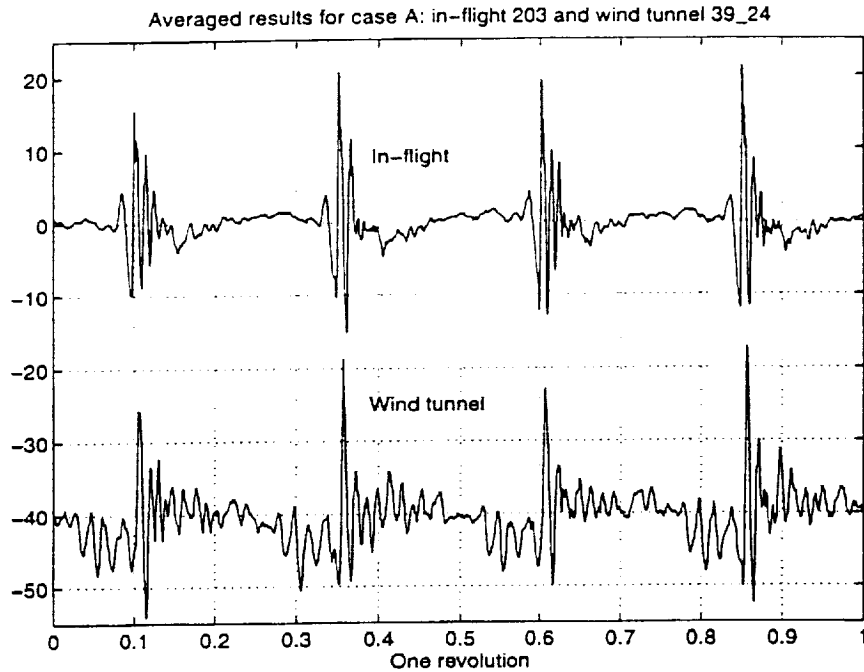


Figure 3.20: Comparing the averaged BVI waveforms for case A: In-flight test 203 and wind tunnel test 39_24. Parameters for in-flight test are: $V_D = 748 \text{ ft/min}$, $\mu = 0.164$, $\alpha = 6.3 \text{ deg}$. Parameters for wind tunnel test are: $V_D = 741 \text{ ft/min}$, $\mu = 0.173$, $\alpha = 5.0 \text{ deg}$

Figure 3.20 shows the comparison between the in-flight test and wind tunnel test for case A (in-flight 203 and wind tunnel 39.24). As detailed in the figure caption, the flight parameters for these two conditions are quite similar, so we expect the averaged BVI signal to be similar as well. As is obvious in the figure, the magnitudes of the major spikes are indeed quite similar for both in-flight and wind tunnel tests. But the detailed BVI waveform from the wind tunnel test is considerably different from the in-flight test. The difference is apparently caused by the boundary effects such as reflections etc. To make the wind tunnel BVI waveform closer to the in-flight test, deconvolution is needed to remove the numerous reflections. This is the topic of the next chapter.

Figure 3.21 compares the averaged results for case B: in-flight 307 and wind tunnel test 48_19. The flight parameters for these two conditions are quite similar, so we also expect the averaged BVI signal to be similar as well. As is clear in the figure, although the magnitude of both data segments are quite comparable, the detailed waveforms are different. The problems with this case are the low BVI signal-to-noise ratio and other wind tunnel effects.

Figure 3.22 shows the comparison between the in-flight test and wind tunnel test for case C (in-flight 315 and wind tunnel 48.18). As detailed in the figure caption, the flight parameters for these two conditions are quite similar, so we expect the averaged BVI signal to be similar as well. As is clear in the figure, the magnitudes of both data segments are quite comparable. Comparisons between the exact BVI waveforms are difficult, but are expected to be feasible after removing the wind tunnel corruption effects from the data set

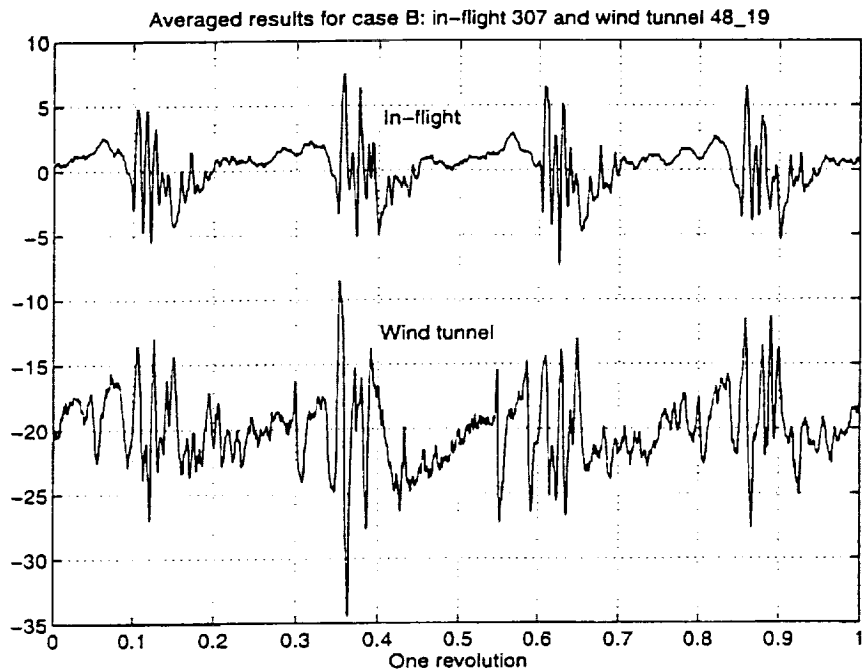


Figure 3.21: Comparing the averaged BVI waveforms for case B: In-flight test 307 and wind tunnel test 48.19. Parameters for in-flight test are: $V_D = 306\text{ft}/\text{min}$, $\mu = 0.203$, $\alpha = 0.1\text{deg}$. Parameters for wind tunnel test are: $V_D = 245\text{ft}/\text{min}$, $\mu = 0.2$, $\alpha = 0\text{deg}$

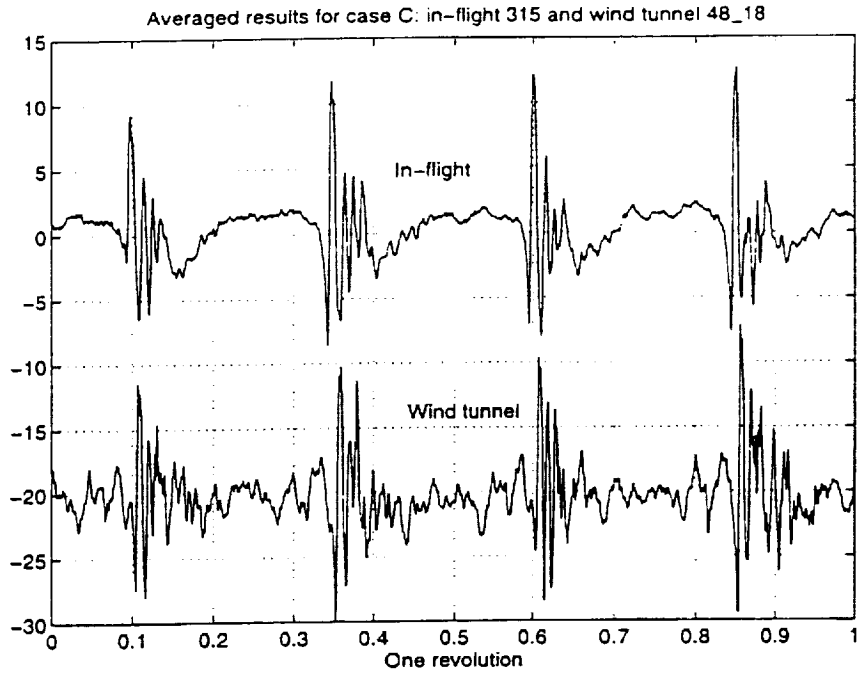


Figure 3.22: Comparing the averaged BVI waveforms for case C: In-flight test 315 and wind tunnel test 48.19. Parameters for in-flight test are: $V_D = 490\text{ft}/\text{min}$, $\mu = 0.245$, $\alpha = -0.4\text{deg}$. Parameters for wind tunnel test are: $V_D = 475\text{ft}/\text{min}$, $\mu = 0.251$, $\alpha = 0\text{deg}$

by deconvolution .

Chapter 4

Further Processing and Analysis of the Wind Tunnel Test Data

The essential goal of this research is to determine the feasibility of using the large wind tunnel (80x120 feet) of NASA-Ames as a way to measure the helicopter blade-vortex-interaction (BVI) acoustic noise. With this goal in mind, it is important to further analyze and process the wind tunnel BVI data.

Compared with the in-flight test, the wind tunnel test is a more controllable testing environment. During the in-flight test, it is hard to maintain a constant tip-path-plane angle, advance ratio, descent rate and a fixed distance between the blade tip and the microphone on the YO-3A airplane. Therefore the in-flight test data usually contains apparent variations from one revolution to another. During the wind tunnel test, these parameters can be accurately controlled, and the data therefore contains far fewer variations from revolution to revolution (see Chapter 3). The wind tunnel test, however, also brings in two unavoidable signal-corrupting mechanisms that are absent from the in-flight test. One is the wind tunnel background noise generated by the large driving fans, the rotating hub (with no blades) and the RTA (rotor-test-apparatus) [5]. The other one is the boundary reflection effects due to the ceiling and the floor as mentioned in Chapter 2. The task of this chapter is to analyze the characteristics of the wind tunnel background noise and the reflected echos, and then examine ways to minimize or remove their effects.

In the following sections, the design of an optimal (Wiener) filter is presented to remove the background noise from the measured BVI data. Filtered results for two test conditions are then given, and a quantitative analysis of the filter performance is presented via the characteristics of the power spectra of the measured data. Following this, ways to cancel the echos by cepstral deconvolution and optimal linear filtering deconvolution are presented and discussed.

4.1 Remove the wind tunnel background noise by optimal filtering

NASA-Ames provided two sets of background noise data that correspond to testing conditions A: 39_24 and B: 48_19 [5]. The background noise was acquired by taking off the rotor

blades from the rotor hub mounted on the RTA while leaving all the other conditions (such as the driving fan speed and the testing rotor RPM etc) unchanged. For a specific testing condition, assume the measured background noise is $w_1(n)$, and the measured BVI data is $x(n) = s(n) + w_2(n)$, where $s(n)$ is the ideal pure BVI signal and w_2 is the background noise embedded within the measured BVI data. A natural question is, can we use the information provided by $w_1(n)$ to cancel the noise $w_2(n)$ to the optimal extent? The answer is yes, provided that $w_1(n)$ carries sufficient statistical information about $w_2(n)$. Although $w_1(n)$ and $w_2(n)$ were acquired at different times, based on simple physical intuition, their statistical properties should be the same. So when designing the optimal Wiener filter in the following, we have assumed that $w_1(n)$ and $w_2(n)$ are statistically identical (denoted simply as $w(n)$).

4.1.1 Design the noise-cancelling optimal filter

A diagram of the filtering system we are developing here is shown in Figure 4.1. The goal is to design a linear filter $h(n)$ so that when passing the measured signal $x(n)$ through the filter, the output signal $\hat{s}(n)$ is the best estimate of the fundamental BVI signal $s(n)$. That is, the design criterion for $h(n)$ is to minimize the total or mean error of $e(n)$.

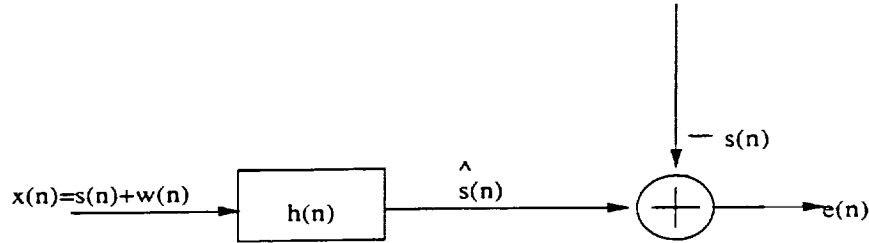


Figure 4.1: A simple diagram of the optimal filtering system

Since this is an off-line data processing problem, not a real time on-line signal processing problem, there is no need to restrain the filter $h(n)$ to be causal. For a causal filter, the estimate $\hat{s}(n)$ is formed as a result of linear prediction using $x(n)$. When the filter is non-causal, then the estimate $\hat{s}(n)$ is a result of averaging the signal $x(n)$. The latter is certainly more stable. Mathematically, we can express the estimate as:

$$\hat{s}(n) = \sum_{i=-L}^L h(i)x(n-i) \quad (4.1)$$

where $h(n)$ has been chosen as a symmetric non-causal filter of length $2L + 1$. The criterion of designing $h(n)$ is to minimize the following total error:

$$J = \sum_{n_b}^{n_e} e^2(n) = \sum_{n_b}^{n_e} \left[\sum_{i=-L}^L h(i)x(n-i) - s(n) \right]^2 \quad (4.2)$$

where n_b and n_e denotes the beginning and ending data points of the specific segment of the measured data $x(n)$ that is used in the equation. By setting the partial derivative of J over

$h(j)$ to zero, we obtain the following normal equation for the filter $h(n)$:

$$[R_{xx}]\underline{h} = \underline{R_{xs}} \quad (4.3)$$

where $[R_{xx}]$ is the $(2L+1) \times (2L+1)$ autocorrelation matrix of the measured data $x(n)$. For a time series of finite length and in reference to equation 4.2, the i -th row and j -th column element of the matrix is:

$$r_{ij} = \sum_{n=n_b}^{n_e} x(n-i)x(n-j) \quad (4.4)$$

$$i, j = -L, -L+1, \dots, L$$

In equation 4.3, $\underline{h} = [h(-L), h(-L+1), \dots, h(L)]^T$ and $\underline{R_{xs}}$ is the cross-correlation vector between the measured signal $x(n)$ and the fundamental BVI signal $s(n)$. In 4.3, the autocorrelation matrix can be readily obtained from the measured data $x(n)$ in the way as shown in 4.4. The key problem is how to find the cross-correlation vector $\underline{R_{xs}}$ since the fundamental BVI signal $s(n)$ is unknown to us. To find this vector, we use $x(n) = s(n) + w(n)$ and therefore we have the following:

$$\begin{aligned} \underline{R_{xs}} &= \underline{R_{ss}} + \underline{R_{sw}} \\ \underline{R_{xx}} &= \underline{R_{ss}} + \underline{R_{ww}} + 2\underline{R_{sw}} \end{aligned} \quad (4.5)$$

Careful examination of the above equation indicates that if $R_{sw} = 0$, then we can calculate $\underline{R_{xs}}$ in terms of the following:

$$\underline{R_{xs}} = \underline{R_{ss}} = \underline{R_{xx}} - \underline{R_{ww}} \quad (4.6)$$

where R_{ww} is the autocorrelation of the background noise and can be readily calculated from the background noise data. The assumption of $R_{sw} = 0$ implies zero cross-correlation or independence between the fundamental BVI signal $s(n)$ and the background noise $w(n)$. This assumption is physically admissible since $s(n)$ and $w(n)$ have different physical origins. The performance of the filter designed through the above equations depends totally on the validity of the assumption of $R_{sw} = 0$. In the following sections, we examine the filtered results for two different test conditions. A quantitative analysis of the performance of the optimal filter is then examined through the power spectra of the measured data.

4.1.2 Filtered result for test condition A:39_24

As shown in Chapter 3, this test condition has the highest BVI signal strength. Figure 4.2 shows a snap shot of the measured BVI data $x(n)$ and the corresponding background noise data $w(n)$.

The background noise appears to consist of mostly periodic narrow band components (bursts of low-amplitude 'impulsive' signals) and some random white noise components. The periodicity of the background noise is no doubt due to the periodicity of the driving fans and the rotor hub. The presence of the background noise in the measured BVI data is particularly obvious when examining the signal characteristics between two neighboring

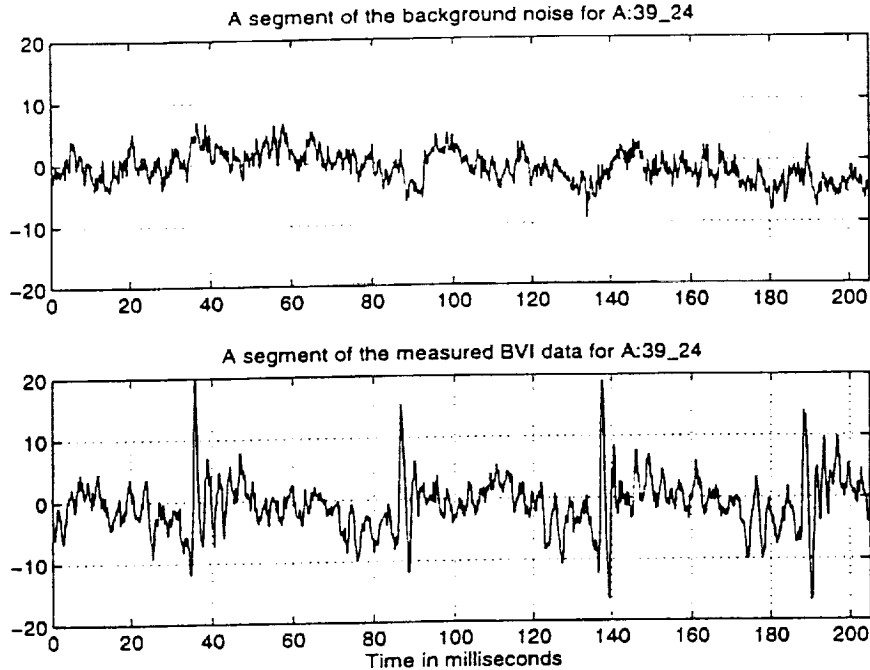


Figure 4.2: A snapshot of the wind tunnel background noise and the measured BVI time series for test condition A: 39_24. Top : background noise. Bottom: BVI data in the wind tunnel

BVI events. Between the two BVI events, the signal level should be low and nearly constant. But as Figure 4.2 shows, the signal level is still quite high and uneven due to the presence of the background noise.

Figure 4.3 shows the comparison between the original BVI data and the filtered result for this test condition A:39_24. The success of the optimal filter in this case is evident. By comparing the filtered and unfiltered results, we see that the optimal filter has satisfactorily lowered the background noise level. The signals between two neighboring BVI events are reduced. The filtered signal looks more like an ideal BVI signal. A 121-tap symmetric non-causal filter was used ($L=60$) in the processing.

Since the optimal filter is so effective, it is natural to ask if we should filter the wind tunnel data first, and then perform averaging on the filtered results according to the method discussed in Chapter 3. Figure 4.4 shows the BVI signal with averaging performed on the data before filtering and after filtering. The averaged BVI events from the unfiltered data still have residual effects from the background noise. That is to say, averaging has not removed the background noise entirely. The noise appears as uneven background. Averaging performed on the filtered result yields an improved wind tunnel BVI signal. The signal level between major BVI events has been reduced. The negative peaks preceding the major BVI event are the reflections from the ceiling, whereas the numerous small peaks following the BVI events are the reflections from the floor (and possibly other reflections as well). The reflected events are more clearly shown in the filtered and then averaged data. It is seen later that this signal makes it easier to perform deconvolution on the data and suppress the

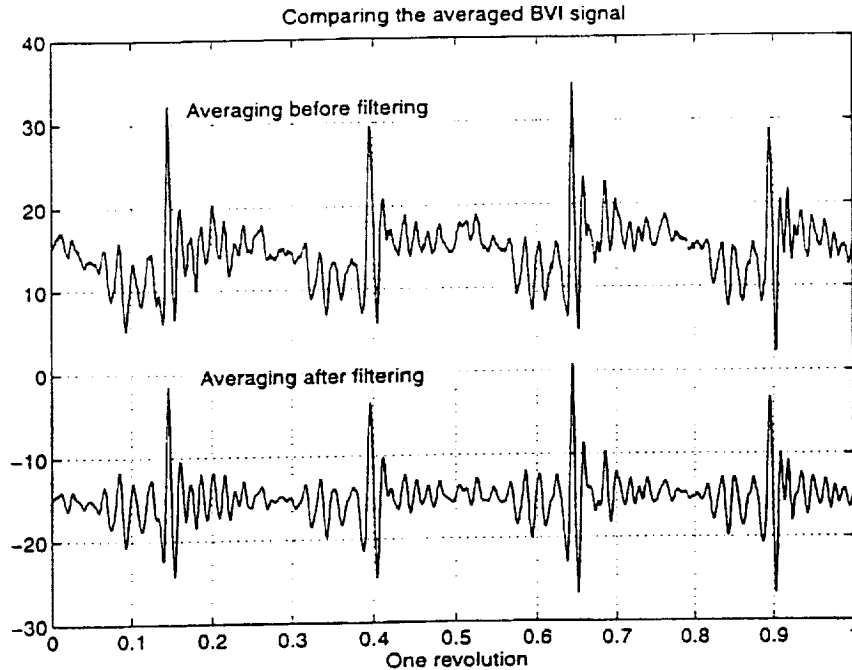


Figure 4.4: Compare the averaged BVI signal from filtered and unfiltered data for test condition A:39.24

see that in this case, the optimal filter failed to improve the signal. In fact, the optimal filter does not remove significant content from the original data. The unfiltered and filtered data segments shown in Figure 4.7 are visually identical. A detailed reason for this problem is given in the next section. Further, since the optimal filter cannot improve the signal in this case, there is no further need to perform averaging on the filtered data.

4.1.4 Power spectra of $x(n)$ and $w(n)$ and their relation to the optimal filter performance

The previous two sections indicate that the optimal filter works well for test condition A, but not so well for test condition B. In this section, we give a more quantitative explanation for this phenomenon using the power spectra of the signal $x(n)$ and $w(n)$.

Notice that the optimal filter is in fact the solution to the following series of linear equations:

$$\sum_{-L}^L R_{xx}(j-i)h(i) = R_{xs}(j) \quad (4.7)$$

$$j = -L, -L+1, \dots, L$$

The left side of the above equation is in convolutional form. So the solution of $h(n)$ in the

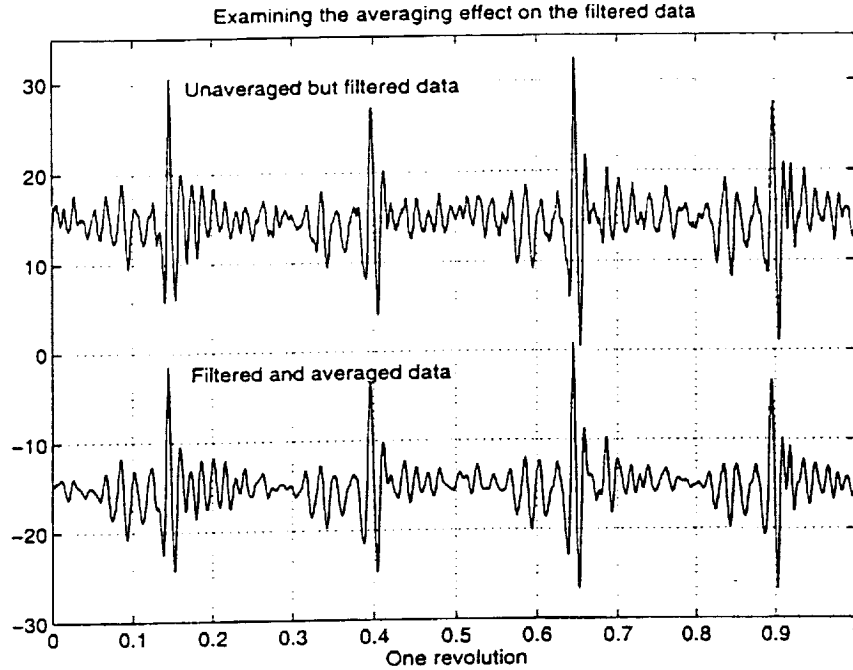


Figure 4.5: Compare the filtered but unaveraged data segment with the filtered and averaged data segment for test condition A:39_24 .

frequency domain is:

$$H(\omega) = \frac{P_{xs}(\omega)}{P_{rx}(\omega)} = \frac{P_{ss}(\omega) + P_{sw}(\omega)}{P_{ss}(\omega) + P_{ww}(\omega) + 2P_{sw}(\omega)} \approx \frac{P_{ss}(\omega)}{P_{ss}(\omega) + P_{ww}(\omega)} \quad (4.8)$$

where $P(\omega)$ is the Fourier transform of the auto or cross correlation function (power spectrum). To obtain the right most side of the above equation, the assumption $R_{sw} = 0$. and therefore, $P_{sw}(\omega) = 0$ was again used. Equation 4.8 indicates that the optimal filter $H(\omega)$ is a simple band-pass or band stop filter when the background noise $w(n)$ and the ideal BVI signal $s(n)$ occupy different frequency bands. For instance, in the frequency band where P_{ss} is large and P_{ww} is small, then $H(\omega) \approx 1$, which is a simple unit gain band pass filter so that as much as possible of the ideal signal $s(n)$ is retained. In the frequency band where P_{ww} is large and P_{ss} is small, then $H(\omega) \approx 0$ which implies a simple band stop filter that will remove as much background noise as possible.

Figure 4.8 shows the power spectra of $w(n)$ and $x(n)$ for test condition A:39_24. The spectra in Figure 4.8 are obtained using the Bartlett [11] method. The whole data section is divided into 10 segments with each segment containing $8212 = 2^{13}$ data points. After Fourier transforming each section, the squared transform amplitudes from each segment is summed and averaged to reduce the estimation variance.

Comparing the two power spectra in Figure 4.8 indicates that the first peak (the $f_1=5\text{Hz}$ component) is present in both the signal $x(n)$ and the noise signal $w(n)$, and the magnitude of the peak in both figures is comparable. This implies that the 5Hz component within the signal $x(n)$ is very likely the background noise. The second peak on the background noise

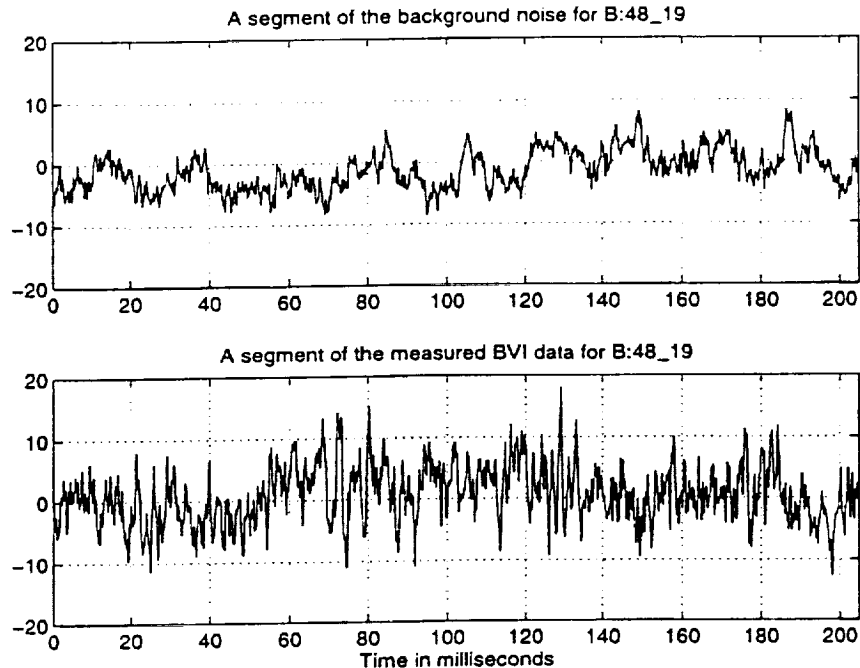


Figure 4.6: A snapshot of the wind tunnel background noise and the measured BVI data for test condition B:48_19. Top : background noise. Bottom: BVI data in the wind tunnel

spectrum ($f_2=45\text{Hz}$ in the top figure) also has a counterpart in the lower figure (the power spectrum of the measured signal $x(n)$) and both have comparable magnitude. But there is an apparent difference between the frequencies (in the top figure $f_2=45\text{Hz}$, in the lower figure, $f_2=40\text{Hz}$).

The character of the signal and noise spectra can be further understood if one considers the wind tunnel fan system and the helicopter rotor. The fans rotate at 180 rpm or 3 Hz and with 15 blades per fan the blade passage frequency is 45 Hz. This is clearly seen in the top of Figure 4.8. However, it appears that either the fan rotation speed or the data sample rate changed for the BVI spectrum seen in the bottom of the figure. The spectral line at 20 Hz in the BVI data is produced by the helicopter rotor. The rotor turns at 300 rpm or 5 Hz and with 4 blades it has a blade passage frequency of 20 Hz. The spectral line of 5 Hz is not explained but it is the rotation frequency for the rotor hub and it is present with and without the BVI data.

Figure 4.8 shows that the background noise occupies the frequency band from 0 to 200Hz, whereas the BVI signal seems to occupy the frequency band from 200Hz up to 500Hz. So we expect the optimal filter to be a high pass filter. It is indeed so as shown in Figure 4.9, where the optimal filter's impulse response and frequency response magnitude are shown. Obviously, below 200Hz, the frequency response magnitude is rather low, indicating that the filter excludes the background noise component. In the frequency band from 200Hz to 500Hz, the magnitude of the frequency response is nearly 1, indicating that the filter passes the BVI components.

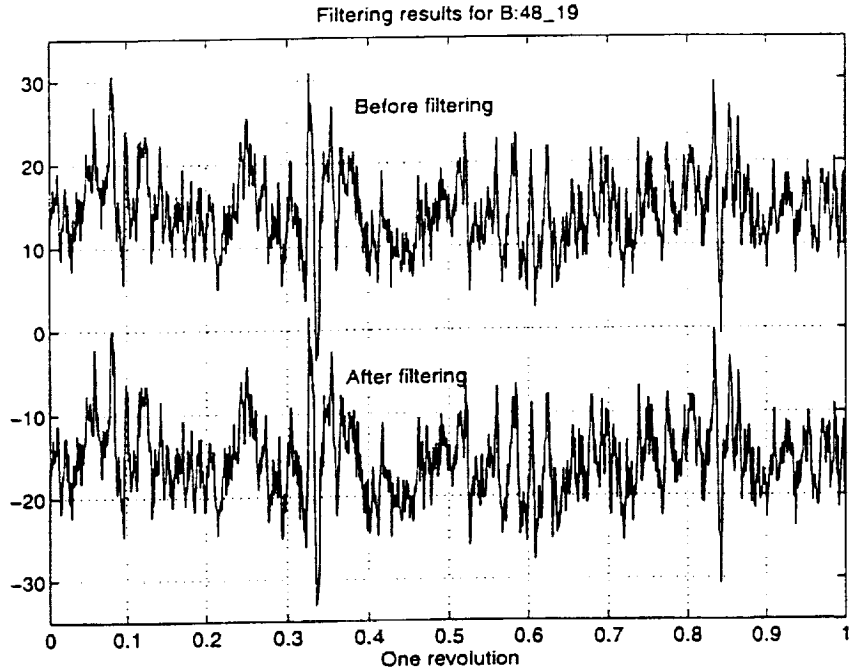


Figure 4.7: Compare the filtered and unfiltered data segments for test condition B:48.19

The situation for test condition B:48.19 is quite different. The power spectra of $x(n)$ and $w(n)$ for this case are shown in Figure 4.10. It's quite disappointing that the background noise components ($f_1=5\text{Hz}$, $f_2=45\text{Hz}$ and $f_3=135\text{Hz}$) shown in the top figure do not have their counterparts in the lower figure (power spectrum of $x(n)$), leading one to question whether these two sets of data were indeed obtained under the same test condition. One possible explanation is that the assumption of $R_{sw} = 0$ is not true for these data. However, it is not evident why this assumption should not be valid for this case. Note we still assume the BVI signal is concentrated in the band between 200 and 500Hz but that it is very weak (low total power) as compared with test condition A:39.24. Uncertainties about the validity of the acoustic data could be lessened if a near-real-time spectrum analyzer were used throughout the measurements to verify unchanging background noise and to monitor the condition of the BVI signal.

In Figure 4.11, both the impulse response and the frequency response magnitude of the optimal filter for test condition B:48.19 are shown. In the frequency band from 0 to 500Hz, the frequency response magnitude is almost unity, indicating that this is essentially an all-pass filter that does not discriminate against the frequency band which the background noise occupies. This also explains the result shown in Figure 4.7, where the filtered and unfiltered results are almost identical since the filter passed all the input signal.

The performance of the optimal filter is in fact determined by the validity of the assumption $R_{sw} = 0$ since the validity of this assumption determines the validity of our way of calculating R_{xs} by the relation $R_{xs} = R_{ss} = R_{xx} - R_{ww}$. The power spectra shown in Figure 4.8 suggest that the power spectrum of $x(n)$ is approximately the sum of the power

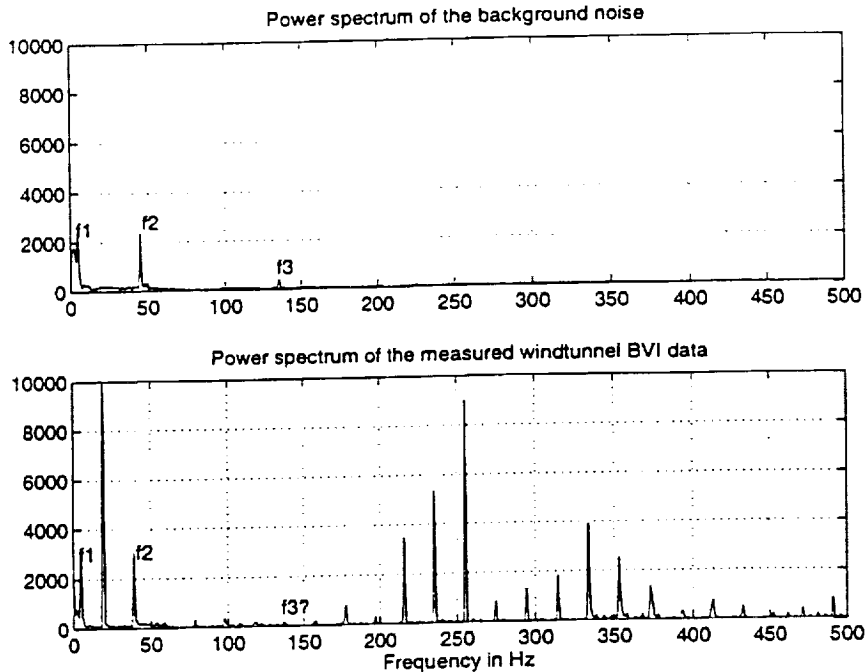


Figure 4.8: Compare the power spectra of the wind tunnel background noise (top figure) and that of the measured BVI signal (lower figure) for test condition A:39_24. For the top figure, $f_1=5\text{Hz}$, $f_2=45\text{Hz}$, and $f_3=135\text{Hz}$. For the lower figure, $f_1=5\text{Hz}$, $f_2=40\text{Hz}$.

spectra of $s(n)$ and $w(n)$ because one can clearly identify the major components of $w(n)$ in $x(n)$. This implies that the cross correlation term R_{sw} is indeed small in this case, therefore, the performance of the optimal filter is indeed 'optimal'. For test condition B:48_19, however, the power spectrum of $x(n)$ does not appear to be a simple sum of $s(n)$ and $w(n)$ since one cannot clearly identify the major components of $w(n)$ in the power spectrum of $x(n)$ (see Figure 4.10). This implies that the assumption $R_{sw} = 0$ is not valid in this case, and therefore, the method we use to calculate $R_{zs} = R_{zx} - R_{zw}$ is not valid, and the 'optimal' filter obtained using this invalid assumption is hence no longer optimal.

4.2 Remove wind tunnel echos by deconvolution

The presence of echos in the wind tunnel BVI data is quite obvious when comparing in-flight test results with the wind tunnel test results. As shown in Figure 4.12, typical wind tunnel measurements contain numerous low-amplitude events preceding and after the major BVI events. A physical mechanism for the occurrence of these has been given in Chapter 2. The event following the major BVI signal is the reflection from the floor. The event preceding the major BVI signal is the reflection from the ceiling. It is obvious that our ability to remove the echos determines, to some extent, whether or not we can use the wind tunnel as a way to measure the BVI signal. However, it has already been shown in Figure 2.17 that altering the measurement geometry could significantly improve the acquired BVI data.

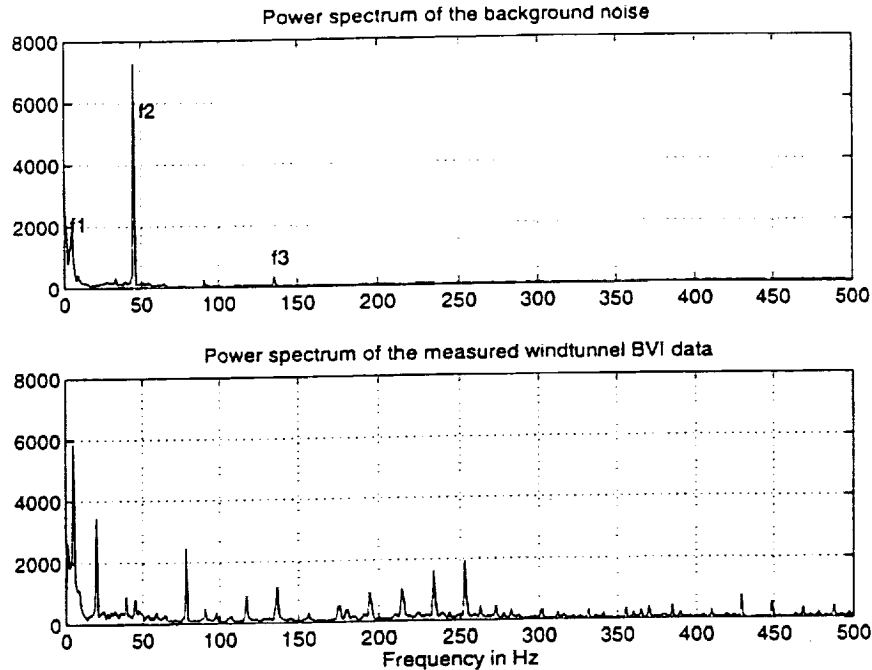


Figure 4.10: Compare the power spectra of the wind tunnel background noise (top figure) and that of the measured BVI (lower figure) for test condition B:48_19

Since we lack quantitative information about the boundary reflection effects of the wind tunnel, our method of removing the echos is based on a “blind-deconvolution” approach similar to that used in geophysical exploration using acoustic signals. All the information has to be extracted from the data itself. In the following sections, we present two methods. the cepstral deconvolution method and an optimal linear deconvolution filter method. Cepstral deconvolution is a nonlinear filtering approach. It works very well for ideal synthetic data with no noise and when the reflectivity sequence meets the minimum phase requirement. But for real data, cepstral deconvolution may fail. In the following, we illustrate the pros and cons of this approach. The optimal linear filter approach is a more pragmatic and more stable approach, although it may not look ‘elegant’ and is more subjective (depending on how we define the desired signal).

4.2.1 Echo removal by cepstral deconvolution

Detailed discussion of cepstral deconvolution can be found in [10] and [13]. Here we only give a simple outline of the crucial points of the cepstrum and homomorphic deconvolution.

A linear filter is effective in separating two signals formed by summation $s(n) = s_1(n) + s_2(n)$. But for a signal formed by convolution $y(n) = x(n) \otimes h(n)$, it is difficult for a linear filter to extract the information of either $x(n)$ or $h(n)$ from the output signal $y(n)$. In the frequency domain, the output is the product of the input and the system: $Y(z) = X(z)H(z)$. If we take the logarithm on both sides of this relation, we form a sum relation $\ln Y(z) = \ln X(z) + \ln H(z)$. This sum relation is now suitable for a linear filter to separate $\ln X(z)$

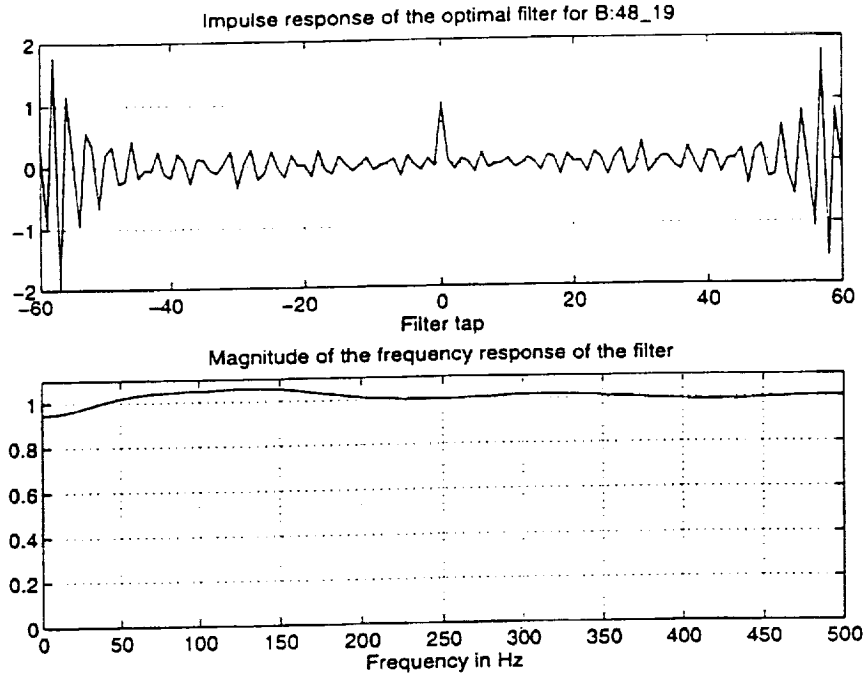


Figure 4.11: Impulse response (top) and frequency response magnitude of the optimal filter designed for test condition B:48_19

and $\ln H(z)$. The cepstrum of a signal $s(n)$ with Z-transform of $S(z)$ is defined as the inverse Z-transform of the logarithm of $S(z)$:

$$c_s(n) = \frac{1}{2\pi j} \oint \ln S(z) z^{n-1} dz \quad (4.9)$$

Based on the above definition, it's obvious that if $y(n) = x(n) \otimes h(n)$, then their cepstra have the following sum relation:

$$c_y(n) = c_x(n) + c_h(n) \quad (4.10)$$

It is then possible to perform filtering on the cepstrum in order to extract $x(n)$ or $h(n)$ from $y(n)$. A simple diagram of the cepstral deconvolution process is shown in Figure 4.13.

Figure 4.14 shows an example of using cepstral deconvolution to extract the input wavelet. In this example, the observed signal is shown in part 'C' of the figure, which is formed by convolving the input wavelet shown in part 'A' with the reflectivity sequence in part 'B'. The reflectivity sequence contains three impulse functions: +1 at time index 0, 0.5 at index 50 and -0.3 at index 450. The observed signal in part 'C' is the only information we know, with nothing being known about the input wavelet or the reflectivity sequence. In this case, the input wavelet extracted from the observed signal using cepstral deconvolution is almost identical to the original input wavelet. The result is shown in part 'D' of the figure.

To better illustrate the key points of cepstral deconvolution, the real part of the observed signal's cepstrum shown in Figure 4.14 part 'C' is shown in the top part of Figure 4.15. There are numerous sharp spikes in the cepstrum. Detailed analysis shows that these spikes

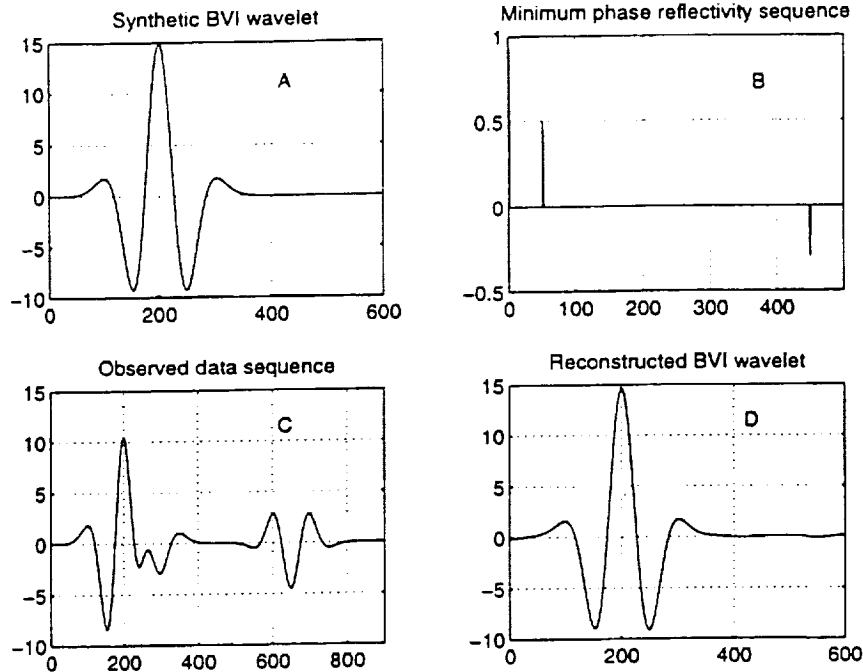


Figure 4.14: An example of cepstral deconvolution showing its success in extracting the input wavelet from the observed signal. A: Input wavelet. B: Reflectivity sequence. C: Observed signal obtained by convolving the signal in A with the signal in B. D: Reconstructed signal after cepstral deconvolution

effect, then the cepstral deconvolution would fail as shown in Figure 4.16. This figure is the same as Figure 4.14 except the reflectivity is changed.

An even more realistic simulation of the wind tunnel reflectivity sequence is shown in part 'B' of Figure 4.17, where the reflectivity of the floor and ceiling are represented not as simple impulses, but as a continuous sequence. This is more realistic because the acoustically treated floor and ceiling have complex frequency-dependent acoustic impedances, and their time domain reflectivity is not a simple impulse, but a continuous sequence. In this case, as Figure 4.17 shows, the cepstral deconvolution once again fails to reconstruct the input wavelet because it can not handle the complicated reflectivity sequences.

Our conclusion from the above results and discussions is that cepstral deconvolution is not applicable to the wind tunnel test data, although it has been used in processing seismic and speech signals with relative success [10] and [12]. In the next section, we pursue a more pragmatic approach in deconvolving the wind tunnel BVI data.

4.2.2 Deconvolving wind tunnel data with an optimal linear filter

The goal of this section is to design a linear filter to remove the echos from the observed wind tunnel BVI data. Ideally, this liner filter is the inverse of the wind tunnel reflectivity filter, therefore it is an IIR filter since its inverse, the reflectivity sequence, is an FIR filter. But for the sake of stability, we restrict the optimal filter to be an FIR filter. The system

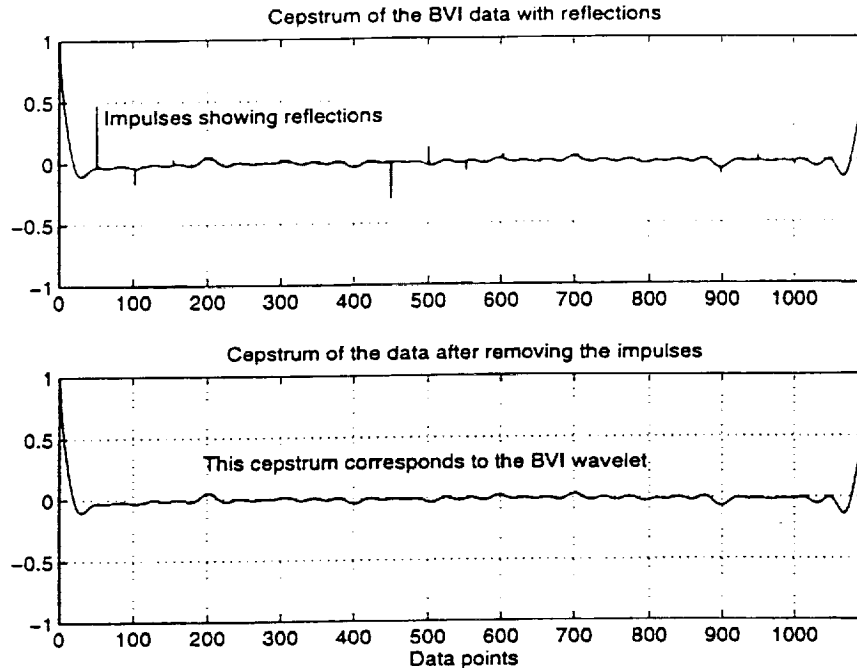


Figure 4.15: Top: Real part of the cepstrum of the observed signal shown in Figure 4.14 part 'C'. Bottom: The same cepstrum after smoothing

diagram for the filter is shown in Figure 4.18.

The criterion for designing the filter $h(n)$ is to make the filtered data sequence approximate a desired data sequence as much as possible. This desired sequence is the BVI sequence with minimal echo content. So, mathematically, the filter $h(n)$ is a solution of the following normal equation obtained by minimizing the total error:

$$[R_{xx}] \underline{h} = \underline{R_{xy}} \quad (4.11)$$

where $\underline{R_{xy}}$ is the cross-correlation vector between the BVI signal with echos ($x(n)$) and the desired BVI signal with no echos ($y(n)$). $[R_{xx}]$ is the autocorrelation matrix of the signal $x(n)$. Now the key point is how to specify the desired BVI signal $y(n)$ (with no echos). To solve this problem, we examine the wind tunnel BVI signal (after background noise removal and averaging) in further detail.

Figure 4.19 shows a single BVI event. Notice that the markers '1' and '2' point to some inflection points on the curve. These inflection points correspond to abrupt phase changes, indicating that, before marker '1', there lies the reflected BVI signal from the ceiling (as a result of the previous BVI event); following marker '2', there lies the floor reflection; and between the markers '1' and '2' is the BVI signal that we desire. Based on this observation, we can design the filter in such a way that the filter minimizes the signal energy outside the markers '1' and '2' (that is, minimizes the reflected events) while maintaining the signal between markers '1' and '2' as intact as possible (preserve a section of the BVI signal that is not corrupted by the echos). Thus, our desired signal $y(n)$ is a windowed version of $x(n)$ (i.e., $y(n) = x(n)w(n)$), where the window function is chosen to have amplitude of one between

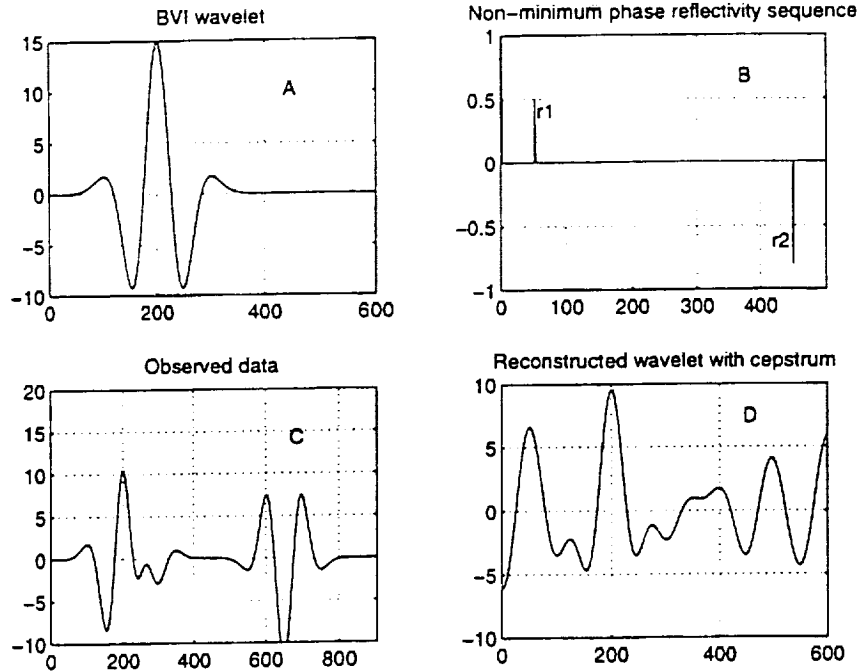


Figure 4.16: An example of cepstral deconvolution showing its failure in extracting the input wavelet from the observed signal because of the non-minimum phase nature of the reflectivity sequence. A: Input wavelet. B: Reflectivity sequence. C: Observed signal obtained by convolving the signal in A with the signal in B. D: Reconstructed signal after cepstral deconvolution

markers '1' and '2' and zero outside the markers. The window is shown in the top part of Figure 4.20 superposed on the measured BVI data sequence. The lower part of the figure shows the windowed signal, which is our desired signal $y(n)$. The principle of choosing the window function is to locate the abrupt phase change points. But this is of course highly subjective, which is a significant drawback of this approach. Once the window is selected, the processing indicated does produce an optimum filter (in a minimum mean square error sense).

After the desired window is chosen, the filter coefficients are then obtained by solving the normal equation. The deconvolved result is then obtained by convolving the original BVI sequence with the filter coefficients. The results are shown in Figure 4.21. The results are quite encouraging, leading one to believe that it is feasible, under the test condition A:39_24 at least, to use the wind tunnel as a way to measure the BVI signal. The BVI sequence after deconvolution is now apparently free of echos. In the figure, a 500-tap FIR filter was used. If a longer filter is used, the result might be better. But the computational cost is also high as it involves the inversion of a large autocorrelation matrix. The results shown in 4.21 are for test condition A:39_24. The data for test condition B:48_19 does not have a high enough signal to noise ratio, so deconvolution is not performed on this data set. For test condition C:48_18, the background noise is not available to us, we therefore can not produce a BVI sequence free of background noise, which is required before performing deconvolution.

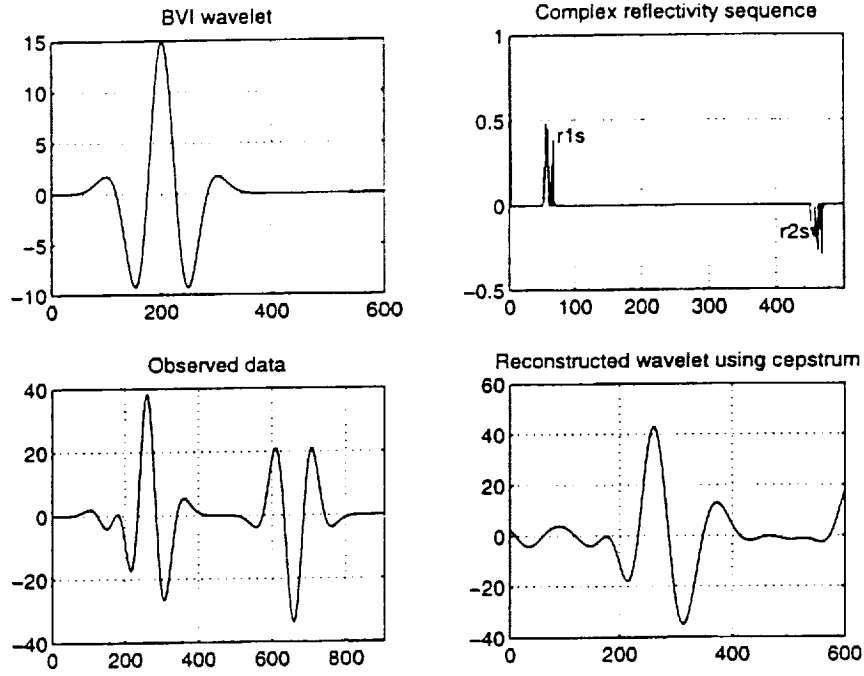


Figure 4.17: An example of cepstral deconvolution showing its failure in extracting the input wavelet from the observed signal because of the complicated reflectivity sequence. A: Input wavelet. B: Reflectivity sequence. C: Observed signal obtained by convolving the signal in A with the signal in B. D: Reconstructed signal after cepstral deconvolution

Figure 4.22 further compares the deconvolved wind tunnel test result with the in-flight test result (averaged data sequence) for test condition A. Our intention is to demonstrate that the deconvolved wind tunnel BVI signal is comparable with the in-flight test result. As is indeed so in Figure 4.22, the essential BVI features in both wind tunnel test and in-flight test are quite similar. The overall magnitude of the wind tunnel test data is smaller. This might be caused by the two filtering processes (one for removing the background noise and one for deconvolution) which are absent from the in-flight test data. The comparison in Figure 4.22 shows that it is feasible to measure the BVI signal inside the wind tunnel, at least for test condition A in which the signal to noise ratio is high enough that two optimal filters can be constructed, one to remove the background noise and one to cancel the echos.

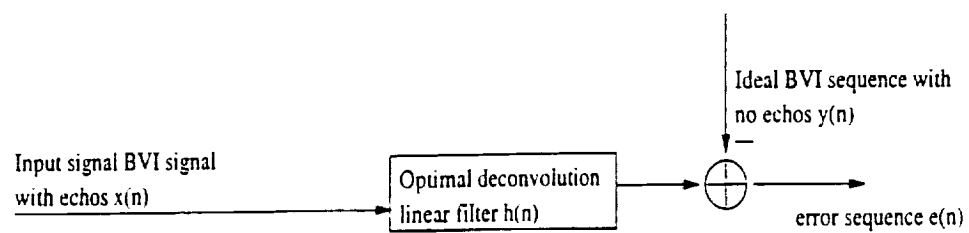


Figure 4.18: A system diagram for the optimal deconvolution FIR filter

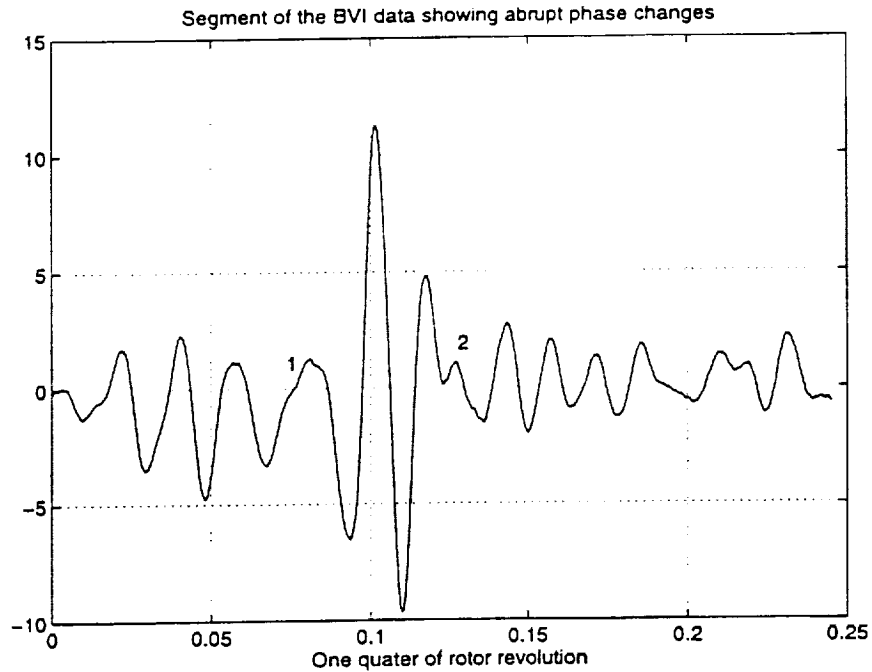


Figure 4.19: One typical BVI event with preceding and following echos. The makers '1' and '2' indicate the abrupt phase changes of the signal

The impulse response and the magnitude of the optimal filter transfer function are shown in Figure 4.23. Ideally, this filter is the inverse of the wind tunnel reflectivity sequence. Since the quantitative information of the reflectivity sequence is unknown, there is no way to give a 'physical' interpretation to the filter.

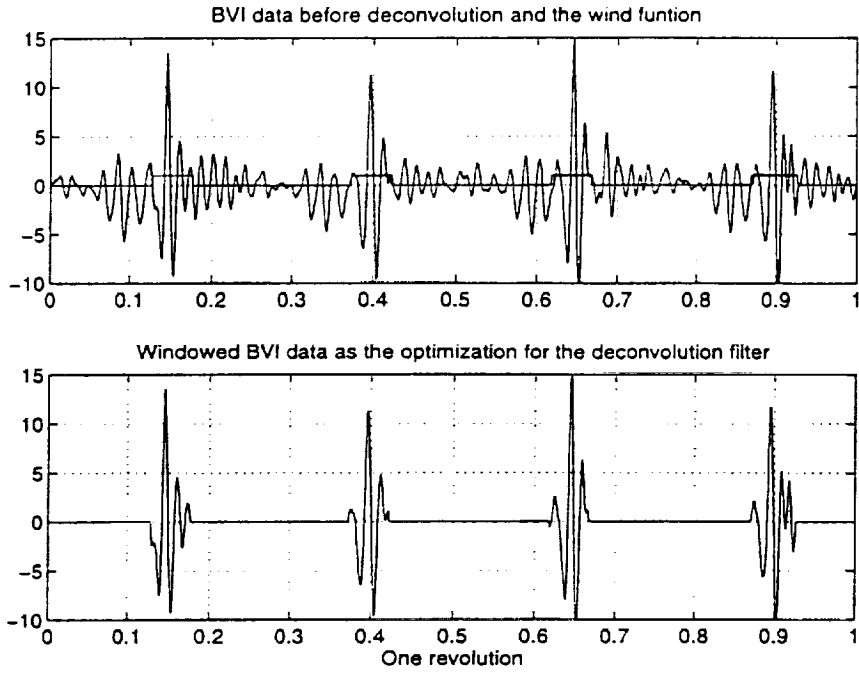


Figure 4.20: A figure showing the original BVI sequence, the window in the background and the windowed sequence used as the desired output for the optimal deconvolution filter

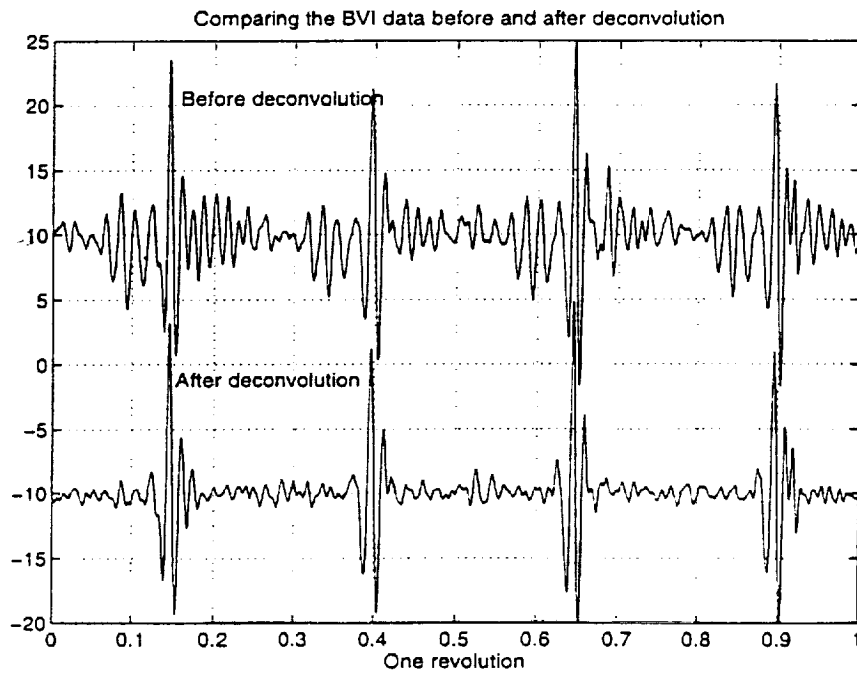


Figure 4.21: Compare the BVI sequence before and after deconvolution by the optimal linear filter. A 500-tap FIR filter was used.

Figure 4.22: Compare the deconvolved wind tunnel BVI sequence with the in-flight test BVI sequence for test condition A

1935
omit and
msg sent under
compare with figure 3.6
Fig 4.21

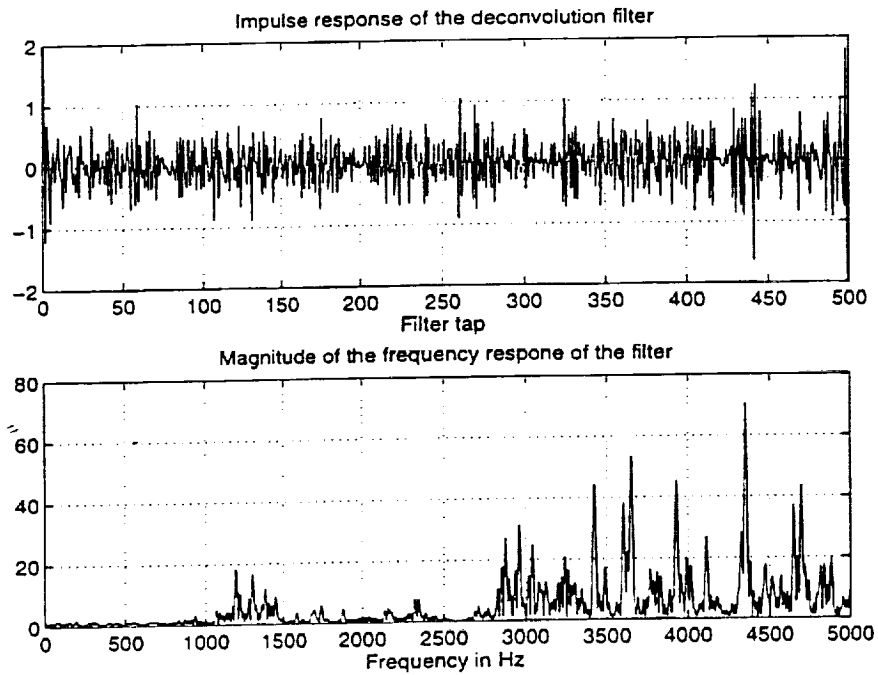


Figure 4.23: Impulse response (top) of the 500-tap optimal FIR filter and its transfer function magnitude (bottom)

Chapter 5

Conclusions and Suggestions for Further Work

5.1 Conclusions

In Chapter 2, we analyzed the BVI signal generating mechanism using a simple mathematical-physical model. Our conclusions from that chapter are:

- On the rotor's advancing side, one blade will have BVI encounters with three vortices shed downward by the preceding three blades. All the BVI encounters take place in the azimuthal angles between 60 and 90 degrees (in the first quadrant of the rotor plane). Each encounter creates one compressional acoustic wavelet corresponding to one positive BVI pulse in the measured data. Therefore, a typical BVI event can contain three positive pulses. The BVI encounter locations depend on the flight conditions such as the advance ratio, descent rate and the tip-path-plane angle etc. Synthetic BVI events generated from this simple BVI encounter model captured the essential features of the measured data for case A, flight 203.
- BVI noise radiation is highly directional. The directivity is perpendicular to the blade span where the blade encounters a vortex. The BVI noise not only radiates in the down-forward direction, but also radiates in the up forward direction. The downward radiation is composed of compressional waves, whereas the upward radiation is composed of dilational waves. This explains the presence of negative peaks in the wind tunnel BVI data. They are caused by the reflection of the upward dilational waves at the ceiling.
- Synthetic BVI events constructed for the wind tunnel configuration showed significant improvement in the direct signal could result from elevating both the rotor hub and the microphone and thereby shifting both the floor reflection and the ceiling reflection away from the desired BVI event.

In Chapter 3, we presented a way to extract the essential BVI feature from the measured data by time domain averaging, analyzed the characteristics of the average data sequence and discussed such issues as the difference of BVI events due to each specific blade. Also the

difference between the BVI events for different flight conditions was discussed and comparison between the in-flight BVI events and the wind tunnel BVI events was made. Our conclusions from that chapter are:

- Time-domain averaging can be used to extract the essential BVI waveforms by enhancing the BVI signals and suppressing the non-BVI random variations. Proper data alignment is crucial for averaging to be effective. Data alignment using the minimal Euclidean distance algorithm is the best method.
- For the in-flight tests, the BVI signals due to the first blade are weaker than those from the other three. Case A (203) has the largest BVI intensity, whereas case B(307) has the weakest BVI signals. The BVI waveform from cases A and C (315) are comparable, the waveforms from case B (307) are very irregular. The BVI signal strength seems to be determined by and proportional to the descent rate.
- For the wind tunnel test, there is no apparent difference between the BVI signals due to different blades. Case A (39_24) has the largest BVI intensity and case B (48_19) has the weakest. The BVI waveforms from cases A and C are comparable, but the waveforms from case B are not comparable. The data sets also indicate that the descent rate is a crucial parameter that determines the BVI strength.
- BVI waveforms from wind tunnel tests are quite different from those of the in-flight tests. The events preceding and following the major BVI events are believed to be caused by ceiling and floor reflections.

In Chapter 4, we presented ways to remove the wind tunnel background noise and echoes from the wind tunnel test data. Our conclusions from that chapter are:

- The wind tunnel background noise can be removed through an optimal linear filter. The key point of designing the filter is the assumption that the BVI signal is uncorrelated with the background noise. The validity of this assumption determines the performance of the optimal filter. It is necessary that a noise signal representative of the noise which contaminated the BVI data be available for constructing the optimal noise reduction filter.
- It was found that cepstral deconvolution can not remove the wind tunnel echoes from the test data. Possible reasons include a non-minimum phase reflectivity sequence or a minimum phase but continuous reflectivity sequence. An optimal linear filter is found to be a better approach for deconvolving the data. The filtered result (after deconvolution) for test condition A:39_24 are satisfactory as the deconvolution process enhanced the major BVI events but suppressed the echoes.
- It is feasible to use the wind tunnel as a way to measure the helicopter BVI signal provided the signal to noise ratio is high enough for the background noise to be successfully removed. The echoes can then be extracted by deconvolution through the use of an optimal linear filter. The filtered and deconvolved wind tunnel data sequence is comparable with the in-flight test result for test condition A (39_24 and 203).

5.2 Suggestions for Further Work

Our suggestions to further work are:

- The quality of the nonaveraged background noise data is crucial. This determines our capability for removing the background noise from the BVI measurement using linear optimal filtering. The background noise and the BVI measurement should be sampled at the same rate and under identical wind tunnel operating conditions. A possible approach is to measure the background noise in real time, i.e., measure the background noise at the same time the BVI signal is measured. This may be accomplished by placing microphones close to the driving fans but far away from the testing rotor so that these microphones only pick up the background noise signal, with minimal possible interference from the rearward radiated BVI signal resulting from the BVI interactions at the blade retreating side.
- A near- real-time spectrum analyzer should be used during all measurements to allow monitoring of both the background noise and the BVI signal. This will alert the operator to changes in the background or the BVI signal. Also, it develops operator familiarity with the effects of changing test conditions on the data.
- Further analysis of expected BVI locations and directivity should be performed prior to making additional BVI measurements. Since flight conditions determine strength, location and directivity of the BVI signal, proper microphone placement (or selection from a group of microphones) should be carefully analyzed prior to establishing the measurement geometry.
- The wind tunnel measurement geometry should be altered to reduce contamination of the direct BVI signal by reflection events. Required modifications could be determined from a reflectivity study conducted in the wind tunnel prior to making new BVI measurements.
- The lining of the floor and the ceiling may have impaired the ability to remove the echoes. The dispersive nature of the lining's reflectivity sequence makes deconvolution particularly difficult. Replacing the lining may cause the BVI data to have stronger echoes, but it's then easier to perform cepstral deconvolution since the hard floor and ceiling have a simple non-dispersive reflectivity of nearly one. Alternatively specific areas on the floor and ceiling where reflections take place can be more effectively treated to minimize these reflections.
- The upward BVI radiation should be verified and treated during the wind tunnel measurements. For example, a few microphones could be placed on the ceiling to measure this upwardly radiated BVI signal to permit removing it from the recorded BVI data.
- Instead of using one microphone at location 6, for example, an array of microphones on a tilted vertical plane should be considered. The strong reception directivity of a microphone array can help overcome the influence of echoes from the floor and the ceiling.